Journal of Fluids and Structures 107 (2021) 103384

Contents lists available at ScienceDirect

Journal of Fluids and Structures

journal homepage: www.elsevier.com/locate/jfs

Dynamics of tethered membranes in inviscid flow

Christiana Mavroyiakoumou *, Silas Alben *

Department of Mathematics, University of Michigan, Ann Arbor, MI 48109, USA

ARTICLE INFO

Article history:
Received 15 June 2021
Received in revised form 13 August 2021
Accepted 25 August 2021
Available online 7 October 2021

Keywords:
Extensible membranes
Flow–structure interactions
Nonlinear instability

ABSTRACT

We investigate the dynamics of membranes that are held by freely-rotating rigid tethers in fluid flows. The tethered boundary condition allows periodic and chaotic oscillatory motions for certain parameter values. We characterize the oscillations in terms of deflection amplitudes, dominant periods, and numbers of local extrema of deflection along the membranes across the parameter space of membrane mass density, stretching modulus, pretension, and tether length. We determine the region of instability and the small-amplitude behavior by solving a nonlinear eigenvalue problem. We also consider an infinite periodic membrane model, which yields a regular eigenvalue problem, analytical results, and asymptotic scaling laws. We find qualitative similarities among all three models in terms of the oscillation frequencies and membrane shapes at small and large values of membrane mass, pretension, and tether length/stiffness.

1. Introduction

There have been many studies of fluid–structure interactions induced by thin flexible bodies. Most of these studies concern flexible beams that are nearly inextensible (Taneda, 1968; Kornecki et al., 1976; Zhang et al., 2000; Zhu and Peskin, 2002; Watanabe et al., 2002; Shelley et al., 2005; Argentina and Mahadevan, 2005; Eloy et al., 2007, 2008; Alben and Shelley, 2008; Alben, 2008; Michelin et al., 2008; Tang et al., 2009a,b; Shelley and Zhang, 2011; Zhao et al., 2012). Another important case that has received somewhat less attention is extensible *membranes* of zero bending modulus. Membranes arise in various biological and technological applications including membrane aircraft and shape-morphing airfoils (Lian and Shyy, 2005; Hu et al., 2008; Stanford et al., 2008; Jaworski and Gordnier, 2012; Piquee et al., 2018; Schomberg et al., 2018; Tzezana and Breuer, 2019), sails (Colgate, 1996; Kimball, 2009), parachutes (Pepper and Maydew, 1971; Stein et al., 2000), membrane roofs (Haruo, 1975; Knudson, 1991; Sygulski, 1996, 1997, 2007), and the wings of flying animals such as bats (Swartz et al., 1996; Song et al., 2008; Cheney et al., 2015). The majority of previous studies of membranes showed that when they are held with their ends fixed in a uniform oncoming fluid flow, they tend to adopt steady shapes with a single hump (that is, when the flat state is unstable) (Song et al., 2008; Mavroyiakoumou and Alben, 2020). In the current work, we show that periodic and chaotic oscillations can occur in a simple physical setup. In our investigation we consider a passive case, i.e., we do not impose heaving or pitching motions (Jaworski, 2012; Tregidgo et al., 2013; Gordnier and Attar, 2014; Tzezana and Breuer, 2019). We also do not have any forcing of oscillations from leading-edge vortex shedding (vortex induced vibrations), which can be important in membranes that are driven by heaving and pitching motions or held at nonzero angle of attack (Rojratsirikul et al., 2011; Jaworski and Gordnier, 2012; Sun et al., 2018).

In Mavroyiakoumou and Alben (2020) we investigated how the membrane dynamics change when using different boundary conditions at the two ends of the membrane. In the first case, fixed–fixed, the membrane ends were held

* Corresponding authors.
E-mail addresses: chrismav@umich.edu (C. Mavroyiakoumou), alben@umich.edu (S. Alben).

https://doi.org/10.1016/j.jfluidstructs.2021.103384
0889-9746/

Table 1
Typical values of parameter ranges relevant to our current model as used in previous membrane studies. Computational ([c]), experimental ([e]), or theoretical ([t]) ranges of the dimensionless body mass density R_1, stretching modulus R_3, and pretension T_0.

Reference	Material	$R_1 = \frac{\rho_s h}{\rho_f L}$	$R_3 = \frac{Eh}{\rho_f U^2 L}$	$T_0 = \frac{\overline{T}}{\rho_f U^2 LW}$
Newman and Païdoussis (1991)[t]	Sail	0–6	–	0–2
Le Maître et al. (1999)[e]	Sail	0–0.8	10^1, 50, 10^2, 500, 10^3	–
Sygulski (2007)[e&t]	Latex rubber	0.1, 1	–	130.6, 217
Jaworski and Gordnier (2012)[c&e]	Latex rubber	2.4	100, 200, 400, 614	4, 10, 20, 30.7
Tiomkin and Raveh (2017)[c]	–	0–80	–	0–6
Nardini et al. (2018)[c]	–	0–60	–	0–3
Das et al. (2020a)[e]	Silicone rubber	2.5–31.25	3.75×10^{-5}–0.04	1–4
Das et al. (2020b)[e]	Silicone rubber	2.5–31.25	3.75×10^{-5}–0.04	1–4
Mavroyiakoumou and Alben (2020)[c&t]	—	10^{-3}–10^2	10^0–10^4	10^{-3}–10^3
Mavroyiakoumou and Alben (2021)[c&t]	—	10^{-3}–10^3	–	$10^{-1.5}$–10^2
Current study[c&t]	—	10^{-4}–10^4	$10^{0.5}$–10^4	10^{-3}–10^2

fixed, as in most previous studies of membrane flutter (Le Maître et al., 1999; Sygulski, 2007; Tiomkin and Raveh, 2017; Nardini et al., 2018). In the second case, fixed–free, we allowed the trailing edge of the membrane to move, but only in the direction perpendicular to the oncoming flow. This gives the free-end boundary condition for a string or membrane in classical mechanics (Graff, 1975; Farlow, 1993), where the membrane end has horizontal slope. The physical meaning of the boundary condition is that the end slides without friction perpendicularly to the membrane's flat equilibrium state (for example, in Farlow (1993) the end is attached to a frictionless, massless ring).

Although well known in classical mechanics, free-end boundary conditions have not been studied much in membrane (as opposed to beam/plate) flutter problems. In Hu et al. (2008), the authors study membrane wings with partially free trailing edges and find that trailing edge fluttering may occur at relatively low angles of attack. Another recent experimental study found that membrane wing flutter can be enhanced by the vibrations of flexible leading and trailing edge supports (Arbós-Torrent et al., 2013). Partially free edges occur also in sails: the shape of a sail membrane can be controlled by altering the tension in cables running along its free edges (Kimball, 2009). Flutter can occur when the tension in these edges is sufficiently low (Colgate, 1996). A related application is to energy harvesting by membranes mounted on tensegrity structures (networks of rigid rods and elastic fibers) and placed in fluid flows (Sunny et al., 2014; Yang and Sultan, 2016). In such cases the membrane ends have some degrees of freedom akin to the free-end boundary conditions defined above.

Related work has studied the dynamics and flutter of membranes and cables under gravity with free ends (Triantafyllou and Howell, 1994; Manela and Weidenfeld, 2017). Here we neglect gravity to focus specifically on the basic flutter problem (Shelley and Zhang, 2011). Without gravity, some restriction on the motion of the free membrane ends is needed to avoid ill-posedness due to membrane compression (Triantafyllou and Howell, 1994). Such a restriction was realized experimentally by Kashy et al. (1997), with the membrane represented by an extensional spring that is tethered by steel wires to vertical supports. The membrane is thus free to move perpendicularly to its flat rest state, but remains stretched between the supports, allowing for stable dynamics. The current paper uses this tethered boundary condition to study membrane dynamics in a fluid flow. We study both small- and large-amplitude dynamics when the membrane is attached to tethers – i.e., inextensible rods that rotate freely – or mounted on springs.

We will show that as the tether length is increased, the membrane dynamics change from static deflections with a single maximum, typical of the fixed–fixed case (similar to the shapes in Newman and Low (1984), Rojratsirikul et al. (2010), Waldman and Breuer (2013, 2017), Nardini et al. (2018), Tzezana and Breuer (2019)) to a wide range of oscillatory motions that have some commonalities with flapping plates and flags (Shelley and Zhang, 2011). We study the stability properties of tethered membranes via a nonlinear eigenvalue problem. The nonlinearity makes it difficult to solve in certain regions of parameter space. Therefore we consider an approximate problem – an infinite membrane mounted on a periodic array of Hookean springs – that is easier to solve and allows us to obtain asymptotic scaling laws for the eigenmodes' dependences on membrane pretension and mass density.

We show in Table 1 typical ranges of membrane parameters – mass density ratios (R_1), stretching rigidities (R_3), and pretensions (T_0) – from previous experimental, theoretical, and computational studies. Newman and Païdoussis (1991) used an infinite periodic membrane model with a low-mode approximation and found that stability is lost through divergence. Le Maître et al. (1999) used a vortex sheet model to study a more complex situation—the motions of a sail membrane under harmonic perturbations of the trailing edge and with randomly perturbed inflow velocities. Sygulski (2007) studied the membrane flutter threshold and divergence modes theoretically, with some experimental validation. Although most works omit specific values of the aspect ratio h/L and the bending modulus $R_2 = Eh^3/(12\rho_f U^2 L^3) = R_3(h/L)^2/12$, an example is given in Jaworski and Gordnier (2012) for a latex rubber, where the aspect ratio is $h/L = 1/750$ and the bending modulus is therefore about a factor of 10^{-7} smaller than R_3. In Jaworski and Gordnier (2012), they studied a heaving and pitching membrane airfoil in a fluid stream numerically at Reynolds number 2500, and found elastic modulus and prestress parameters that led to enhanced thrust and propulsive efficiency. Tiomkin and Raveh (2017)

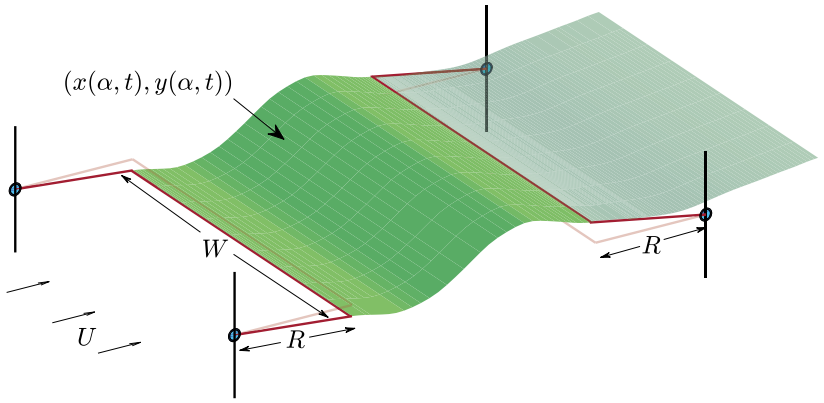

Fig. 1. Schematic diagram of a flexible membrane (dark green surface) at an instant in time. U is the oncoming flow velocity and W is the membrane's spanwise width. The leading edge and the trailing edge of the membrane is attached to inextensible rods (red frames) that rotate freely about their hinged ends (small black/blue circles). There is also a vortex wake (light green surface) emanating from the membrane's trailing edge. (For interpretation of the references to color in this figure legend, the reader is referred to the web version of this article.)

presented a more detailed flutter threshold calculation using an inviscid, small amplitude vortex sheet model. Nardini et al. (2018) compared a reduced-order model with direct numerical simulations to study the effect of Reynolds number on the flutter stability threshold and small-amplitude membrane deflection modes. Das et al. (2020a) modeled the material properties of ultrasoft dielectric elastomers over a wide range of elastic properties, prestretch, and thicknesses. They measured the mechanical response of the silicone membranes and found that stiffer membranes harden at lower stretch ratios due to the increased fraction of polymer chains in them. Das et al. (2020b) studied the deformations, forces, and flow fields associated with a highly compliant membrane disk placed head-on in a uniform flow field. With increasing flow velocity, the membrane deforms hyper-elastically into parachute-like shapes. A resulting drag increase correlates with the unsteady fluid–structure interactions between the membrane and the flow. In the present study, we set R_2 to zero and study the dynamics of tethered membranes over wide ranges of the remaining parameters—R_1, R_3, and T_0—as well as the tether length or stiffness. Here unsteady dynamics are possible because, unlike in previous studies, the membrane is attached to inextensible rod tethers whose lengths set the transition between steady and unsteady motions.

The paper is structured as follows. We begin in Section 2 by presenting the membrane and vortex-sheet model and in Section 2.1 we present the boundary conditions when the membranes are attached to inextensible-rod tethers. In Section 3 we present the results in the large-amplitude regime for this boundary condition. In Sections 3.1 and 3.2 we study the related case of membranes mounted on Hookean springs. In Section 4 we present a linearized, small-amplitude version of our model and study the stability properties (Section 4.1). We then study the stability behavior of an infinite periodic membrane mounted on a periodic array of springs and propose asymptotic scaling laws (Section 5). Finally, in Section 6, we summarize our findings.

2. Membrane and vortex-sheet model

We model the dynamics of an extensible membrane that is nearly aligned with a two-dimensional background fluid flow that has speed U in the far field (see Fig. 1). The membrane is shown as a dark green surface with the vortex wake (light green surface) emanating from its trailing edge. Each membrane end is attached to a massless, open rigid frame of inextensible rods (red solid lines) that pivots freely at the hinges shown by small black/blue circles in Fig. 1 and therefore the membrane's ends are constrained to move along circles of radius R centered at the hinges. The motions of the membrane and open rod frames are assumed to be invariant in the spanwise direction (along W), and the effect of gravity is neglected for simplicity. The four clamping poles (black lines) at the end of the rod frame away from the membrane are sufficiently thin that their influence on the fluid flow is assumed to be negligible.

The membrane and flow models are the same as in Mavroyiakoumou and Alben (2020) but we repeat them briefly for completeness. The membrane dynamics are described by the unsteady extensible elastica equation with body inertia, stretching resistance, and fluid pressure loading, obtained by writing a force balance equation for a small section of membrane that lies between material coordinates α and $\alpha + \Delta\alpha$:

$$\rho_s h W \partial_{tt}\zeta(\alpha,t)\Delta\alpha = T(\alpha+\Delta\alpha)\hat{\mathbf{s}} - T(\alpha,t)\hat{\mathbf{s}} - [p]^{+}_{-}(\alpha,t)\hat{\mathbf{n}}W(s(\alpha+\Delta\alpha,t)-s(\alpha,t)). \tag{1}$$

Here ρ_s is the mass per unit volume of the undeflected membrane, h is the membrane's thickness, and W its spanwise width, all uniform along the length. In Eq. (1), $\zeta(\alpha,t) = x(\alpha,t) + iy(\alpha,t)$ denotes the membrane position in the complex plane, parameterized by the material coordinate α, $-L \le \alpha \le L$ (L is half the initial length) and time t. T is the tension in

the membrane, $[p]^{+}_{-}$ is the pressure jump across it, $s(\alpha, t)$ is the local arc length coordinate, and the unit vectors tangent and normal to the membrane are $\hat{\mathbf{s}} = \partial_\alpha \zeta(\alpha, t)/\partial_\alpha s(\alpha, t) = e^{i\theta(\alpha,t)}$ and $\hat{\mathbf{n}} = i\hat{\mathbf{s}} = ie^{i\theta(\alpha,t)}$, respectively, with $\theta(\alpha, t)$ the local tangent angle and $\partial_\alpha s$ the local stretching factor. We use $+$ to denote the side towards which the membrane normal $\hat{\mathbf{n}}$ is directed, and $-$ for the other side. However, for the remainder of this paper, we drop the $+$ and $-$ for ease of notation.

Dividing Eq. (1) by $\Delta\alpha$ and taking the limit $\Delta\alpha \to 0$, we obtain

$$\rho_s h W \partial_{tt}\zeta(\alpha, t) = \partial_\alpha(T(\alpha, t)\hat{\mathbf{s}}) - [p](\alpha, t) W \partial_\alpha s \hat{\mathbf{n}}, \tag{2}$$

where the membrane tension $T(\alpha, t)$ is given by linear elasticity (Carrier, 1945; Narasimha, 1968; Nayfeh and Pai, 2008) as

$$T(\alpha, t) = \overline{T} + EhW(\partial_\alpha s(\alpha, t) - 1). \tag{3}$$

Here E is the Young's modulus and $\overline{T}$ is the tension in the initial, undeflected equilibrium state. After nondimensionalizing length by L, time by L/U, and pressure by $\rho_f U^2$, where ρ_f is the density of the fluid and U is the oncoming flow velocity, Eq. (2) becomes the nonlinear, extensible membrane equation

$$R_1 \partial_{tt}\zeta - \partial_\alpha((T_0 + R_3(\partial_\alpha s - 1))\hat{\mathbf{s}}) = -[p]\partial_\alpha s \hat{\mathbf{n}}. \tag{4}$$

In Eq. (4), $R_1 = \rho_s h/(\rho_f L)$ is the dimensionless membrane mass, $T_0 = \overline{T}/(\rho_f U^2 LW)$ is the dimensionless pretension, and finally, $R_3 = Eh/(\rho_f U^2 L)$ is the dimensionless stretching rigidity. We use Eq. (4) to study large-amplitude motions in Section 3. We use a linearized, small-amplitude version to study membrane stability in Sections 4 and 5.

We express the 2D flow past the membrane using $z = x + iy$, the complex representation of the xy flow plane. The complex conjugate of the fluid velocity at any point z not on the vortex sheets is a sum of the horizontal background flow with speed unity and the flow induced by the bound and free vortex sheets,

$$u_x(z) - iu_y(z) = 1 + \frac{1}{2\pi i}\int_{-1}^{1} \frac{\gamma(\alpha, t)}{z - \zeta(\alpha, t)} \partial_\alpha s \mathrm{d}\alpha + \frac{1}{2\pi i}\int_0^{s_{\max}} \frac{\gamma(s, t)}{z - \zeta(s, t)} \mathrm{d}s, \tag{5}$$

where s is the arc length along the free sheet starting at 0 at the membrane's trailing edge and extending to $s_{\max}$ at the free sheet's far end. To determine the bound vortex sheet strength γ we require that the fluid does not penetrate the membrane, which is known as the kinematic boundary condition. Here γ represents the jump in the component of the flow velocity tangent to the membrane from the $-$ to the $+$ side, i.e., $\gamma = -[(u_x, u_y) \cdot \hat{\mathbf{s}}]$. The normal components of the fluid and membrane velocities are equal along the membrane:

$$\mathrm{Re}(\hat{\mathbf{n}}\partial_t \overline{\zeta}(\alpha, t)) = \mathrm{Re}\left(\hat{\mathbf{n}}\left(1 + \frac{1}{2\pi i}\int_{-1}^{1} \frac{\gamma(\alpha, t)}{z - \zeta(\alpha, t)} \partial_\alpha s \mathrm{d}\alpha + \frac{1}{2\pi i}\int_0^{s_{\max}} \frac{\gamma(s, t)}{z - \zeta(s, t)} \mathrm{d}s\right)\right), \tag{6}$$

where $\hat{\mathbf{n}}$ is written as a complex scalar. Solving Eq. (6) for γ requires an additional constraint that the total circulation is zero for a flow started from rest. At each instant the part of the circulation in the free sheet, or alternatively, the strength of γ where the free sheet meets the trailing edge of the membrane, is set by the Kutta condition which makes velocity finite at the trailing edge. At every other point on the free sheet, γ is set by the criterion that circulation (the integral of γ) is conserved at fluid material points of the free sheet. The vortex sheet strength $\gamma(\alpha, t)$ is coupled to the pressure jump $[p](\alpha, t)$ across the membrane using a version of the unsteady Bernoulli equation written at a fixed material point on the membrane:

$$\partial_\alpha s \partial_t \gamma + \partial_\alpha(\gamma(\mu - \tau)) + \gamma(\partial_\alpha \tau - \nu\kappa\partial_\alpha s) = \partial_\alpha[p], \tag{7}$$

where μ is the average flow velocity tangent to the membrane, τ and ν are the tangential and normal components of the membrane velocity, respectively, and $\kappa(\alpha, t) = \partial_\alpha\theta/\partial_\alpha s$ is the membrane's curvature. At the trailing edge, $[p]|_{\alpha=1} = 0$. The derivation of Eq. (7) can be found in Mavroyiakoumou and Alben (2020, Appendix A).

2.1. Boundary conditions: inextensible-rod tethers

A slice through the membrane and rod frame in the 2D flow plane is shown schematically in Fig. 2. The rod frames pivot freely about the points $(-R, 0)$ and $(2+R, 0)$, respectively. Because the frames are inextensible, the membrane ends are constrained to move along circular arcs of radius R. This is enforced by requiring

$$(x_{-1} - (-R))^2 + y_{-1}^2 = R^2 \quad \text{and} \quad (x_1 - (2 + R))^2 + y_1^2 = R^2, \tag{8}$$

for all time, where $x_{\pm 1} = x(\pm 1, t)$ and $y_{\pm 1} = y(\pm 1, t)$ are four unknowns that denote the x- and y-coordinates of the membrane ends, respectively. Two equations for the four unknowns are (8) and the remaining two equations require the membrane and rod frames to be tangent where they meet:

$$\left.\frac{\partial_\alpha y}{\partial_\alpha x}\right|_{\alpha=-1} = \frac{y_{-1} - 0}{x_{-1} - (-R)} \quad \text{and} \quad \left.\frac{\partial_\alpha y}{\partial_\alpha x}\right|_{\alpha=1} = \frac{0 - y_1}{(2 + R) - x_1}, \tag{9}$$

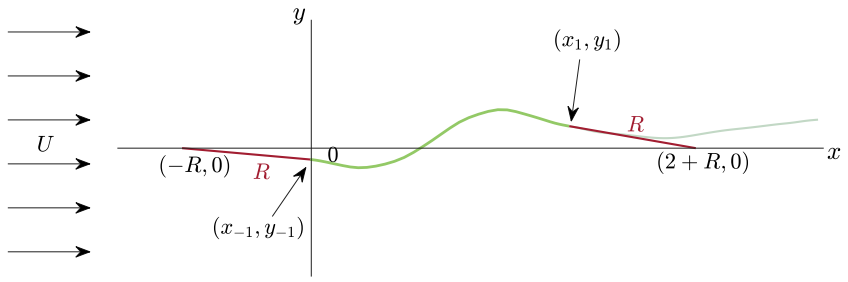

Fig. 2. Slice through the membrane in Fig. 1. Schematic diagram of a flexible membrane (green line) at an instant in time. The leading edge of the membrane with position $(x(-1,t), y(-1,t))$ is attached to an inextensible rod frame (red line) whose motion is restricted to a circle of radius R (length of rod frame) and whose other end is fixed at $(-R, 0)$ for all time. The membrane's trailing edge with position $(x(1,t), y(1,t))$ is attached to another rod frame whose other end is fixed at $(2+R, 0)$ for all time. There is also a vortex wake emanating from the membrane's trailing edge (light green line). (For interpretation of the references to color in this figure legend, the reader is referred to the web version of this article.)

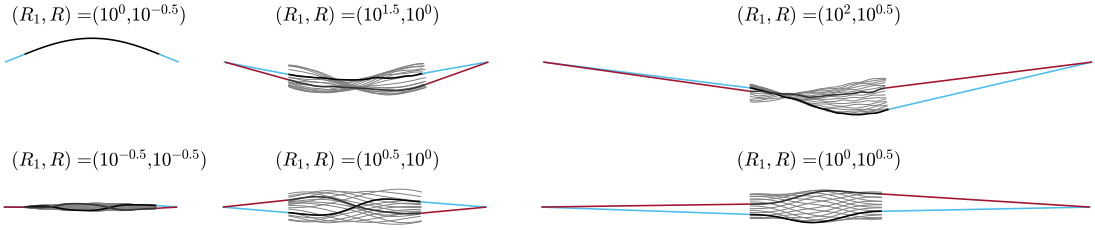

Fig. 3. Examples of membrane (black) and rod (red and blue) snapshots at two different times, superposed on a larger set of membrane snapshots (gray) within a period. Each column corresponds to a rod length R: $10^{-0.5}$ (left column), 10^0 (middle column), and $10^{0.5}$ (right column). Here $R_3 = 10^{1.5}$ and $T_0 = 10^{-2}$. (For interpretation of the references to color in this figure legend, the reader is referred to the web version of this article.)

again for all time. Eqs. (9) follow from balancing the forces on an infinitesimal length of membrane near the membrane ends; because its mass is infinitesimal, the tension forces on it from the rods and from the adjacent portion of the membrane must be aligned. The rod tether length R is an important parameter that influences the dynamics of the membrane. With short rods ($R \to 0$), we will show that the membrane dynamics are similar to fixed–fixed membranes, whereas with longer rods the dynamics resemble free–free membranes but without the large-scale translational motions seen in Mavroyiakoumou and Alben (2020).

3. Large-amplitude results

We simulate the membrane starting from an initial condition in which the membrane is perturbed from the flat horizontal equilibrium state: it has a linear profile with a small nonzero slope,

$$\zeta(\alpha, 0) = (\alpha + 1)(1 + i\sigma), \tag{10}$$

for $\sigma = 10^{-3}$. We evolve the membrane and vortex sheet wake forward in time using a numerical method similar to those in Alben (2009) and Mavroyiakoumou and Alben (2020).

In Fig. 3 we show snapshots of membranes and rods for a fixed stretching rigidity ($R_3 = 10^{1.5}$) and pretension ($T_0 = 10^{-2}$), at six pairs of (R_1, R) values that give typical dynamics. In each case, two of the snapshots show the rods (blue in one and red in the other) together with the membranes (black lines). The remaining 16 snapshots show only the membranes (gray lines), equally spaced in time within a period of motion. R increases from left to right: $10^{-0.5}$ (left column), 10^0 (middle column), and $10^{0.5}$ (right column). The membrane deflection may be very small, particularly at small R_1 (bottom left case), and may be steady, particularly at small R (top left case). In the bottom row, middle column case (i.e., $R_1 = 10^{0.5}$ and $R = 10^0$) and in the bottom row, right column case (i.e., $R_1 = 10^0$ and $R = 10^{0.5}$) it is evident that the inextensible rods may deflect upwards or downwards.

We characterize the large-amplitude dynamics using three main quantities. One is the time-averaged deflection of the membrane, defined as

$$\langle y_{\text{defl}} \rangle \equiv \frac{1}{t_2} \int_{t_1}^{t_1+t_2} \left(\max_{-1 \le \alpha \le 1} y(\alpha, t) - \min_{-1 \le \alpha \le 1} y(\alpha, t) \right) \mathrm{d}t. \tag{11}$$

Here, as in Mavroyiakoumou and Alben (2020), t_1 and t_2 are sufficiently large (typically 50–100) that $\langle y_{\text{defl}} \rangle$ changes by less than 1% with further increases in these values. So, $\langle y_{\text{defl}} \rangle$ is the maximum membrane deflection minus the minimum membrane deflection, averaged over time.

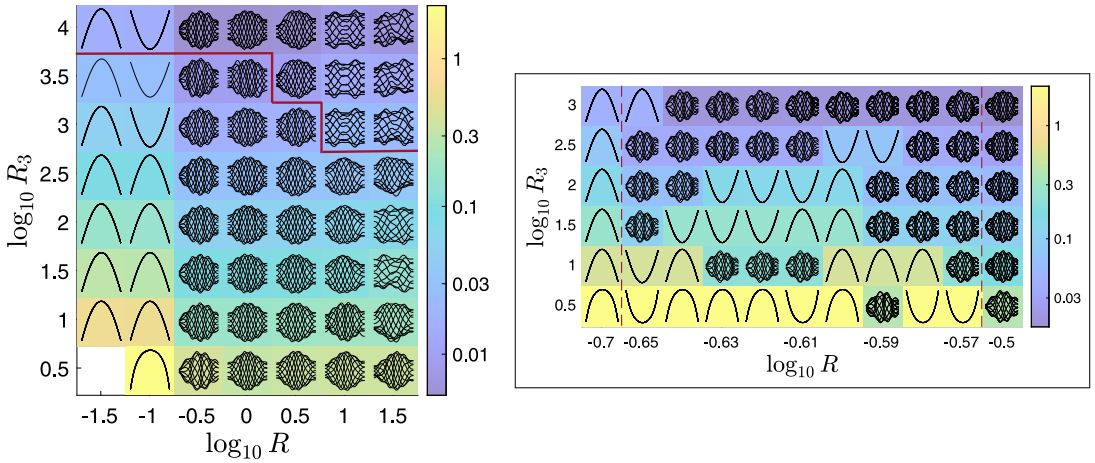

Fig. 4. (Inextensible rods) Snapshots of large-amplitude membrane motions in R–R_3 space for fixed $T_0 = 10^{-2}$ and $R_1 = 10^{-0.5}$. Colors represent the time-averaged deflection of the membranes defined by Eq. (11). For rods with length $R \leq 10^{-1}$ the membranes behave similarly to those with fixed–fixed ends, yielding a single hump solution, whereas when $R \geq 10^{-0.5}$ the membranes oscillate as in some cases with free–free ends. At each (R, R_3) value, the set of snapshots is scaled to fit within a colored rectangle centered at that value and normalized by the maximum deflection of the snapshots to show the motions more clearly. The red solid line separates membranes with $m = 40$ points (above) and $m = 120$ points (below). In the framed figure we look at a finer grid between $R = 10^{-0.7}$ and $10^{-0.5}$, to investigate dynamics near the transition between the single-hump solution and the flapping state occurs. The red dashed lines indicate a jump in the increment of R values. (For interpretation of the references to color in this figure legend, the reader is referred to the web version of this article.)

The second quantity used to characterize the large-amplitude dynamics is the time period. This is computed using the peak frequency in the power spectrum computed using the fast Fourier transform (`fft` function in MATLAB). The power spectrum is obtained from a time series of the membrane's midpoint when the membrane has reached steady-state large-amplitude dynamics. The third quantity is the time-averaged number of zero crossings along the membrane, computed using the same temporal data as the power spectrum. Apart from the number of zero crossings, we also use the time-averaged number of local extrema as a different measure of the 'waviness' of the membrane shape.

In Fig. 4 we show typical membrane snapshots in R–R_3 space, while fixing $T_0 = 10^{-2}$ and $R_1 = 10^{-0.5}$. At each (R, R_3) value, the set of snapshots is normalized by the maximum deflection of the snapshots to show the motions more clearly and scaled to fit within a colored rectangle at the (R, R_3) value. Each snapshot has the corresponding R value at its horizontal midpoint, and the R_3 value at its average vertical position. Colors represent the time-averaged deflection defined by Eq. (11). In the lower-left corner the snapshots are omitted because steady-state membrane motions were not obtained. Two main types of membrane behaviors are seen: at small R, a steady single-hump shape that is fore–aft symmetric, similar to membranes that have both the leading and trailing edges fixed at zero deflection; at moderate-to-large R, an oscillatory motion. The framed panel on the right-hand side of Fig. 4 shows the transition between these states in finer detail, between $R = 10^{-0.65}$ and $10^{-0.57}$. The red dashed lines show where larger increments of R are taken, from $10^{-0.65}$ to $10^{-0.7}$ (where only single hump solutions are obtained for any R_3) and from $R = 10^{-0.57}$ to $10^{-0.5}$ (where only flapping membranes are observed, for any R_3). In the framed panel we see that the initial condition of nonzero slope [Eq. (10)] may evolve to single-hump shapes that are concave up, concave down, or to oscillatory motions when R is changed slightly. In the left panel, the oscillatory motions are mostly close to periodic and fore–aft symmetric, with some deviations particularly at $R = 10^{-0.5}$ and $10^{1.5}$, where a less wavy shape becomes more common.

For very large stretching rigidity $R_3 \gtrsim 10^3$ the code reaches the steady-state regime only if we decrease the membrane discretization size to $m = 40$ (from $m = 120$ below the red dividing line). As we observed in Mavroyiakoumou and Alben (2020), in many cases varying the stretching rigidity R_3 alters the overall deflection magnitudes but leaves the membranes' shapes nearly unchanged.

In Fig. 5 we show how the time-averaged deflection quantitatively depends on R_3 at several fixed values of $R \in \{10^{-1.5}, 10^{-1}, \ldots, 10^{1.5}\}$, for $R_1 = 10^{0.5}$ and $T_0 = 10^{-2}$ here. The $\langle y_{\text{defl}} \rangle \sim R_3^{-1/2}$ dependence at large R_3 is the same for other mass ratios from $R_1 = 10^{-0.5}$ to $R_1 = 10^2$, again with $T_0 = 10^{-2}$. This was observed also for fixed–fixed, fixed–free, and free–free membranes in Mavroyiakoumou and Alben (2020). We include the explanation for how the scaling $\langle y_{\text{defl}} \rangle \sim R_3^{-1/2}$ arises from the y-component of the membrane equation [Eq. (4)] with small deflections. We assume that $\partial_\alpha y \ll 1$ and $\partial_\alpha x \approx 1$. Then $\partial_\alpha s - 1 = \sqrt{(\partial_\alpha x)^2 + (\partial_\alpha y)^2} - 1 \approx \partial_\alpha y^2/2$ and $\hat{s}_y \approx \partial_\alpha y$. With these approximations, the y-components of the T_0 and R_3 terms in Eq. (4) are linear and cubic in deflection, respectively:

$$\partial_\alpha(T_0 \hat{s}_y) \approx T_0 \partial_{\alpha\alpha} y; \quad \partial_\alpha(R_3(\partial_\alpha s - 1)\hat{s}_y) \approx R_3 \partial_\alpha((\partial_\alpha y)^3/2). \tag{12}$$

The R_1 term that multiplies $\partial_{tt} y$ is also linear in deflection. The pressure jump is linear in the bound vortex sheet strength because the left-hand side of Eq. (7) $\approx \partial_t \gamma + \partial_\alpha \gamma$ with small deflections. The bound vortex sheet strength is linear in the

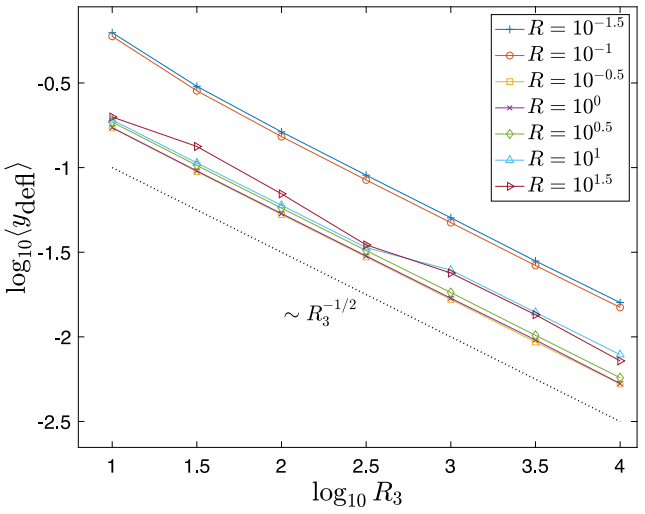

Fig. 5. (Inextensible rods) Time-averaged deflections of the membranes (defined by Eq. (11)) versus R_3 for various R and fixed $R_1 = 10^{0.5}$, $T_0 = 10^{-2}$. The dotted black line indicates the scaling $R_3^{-1/2}$.

deflection by the linearized version of Eq. (6),

$$\partial_t y(\alpha, t) \approx \frac{1}{2\pi}\int_{-1}^{1} \frac{\gamma(\alpha', t)}{x(\alpha, t) - x(\alpha', t)}\,\mathrm{d}\alpha' - \frac{1}{2\pi}\int_{0}^{\Gamma_+(t)} \frac{x(\alpha, t) - x(\Gamma', t)}{(x(\alpha, t) - x(\Gamma', t))^2 + \delta(\Gamma', t)^2}\,\mathrm{d}\Gamma', \tag{13}$$

in which the second integral consists of bound vorticity advected from the trailing edge, so it has the same dependence on deflection as the bound vorticity. Here, with small deflections, we have assumed that $\partial_\alpha x \approx 1$, and then the linearization is the same as in Alben and Shelley (2008), Mavroyiakoumou and Alben (2020). Without viscous stresses, horizontal membrane deformations arise only through nonlinear terms in the elastic and pressure forces associated with large deflections, so it is reasonable to neglect them, and this is consistent with the simulation results. Balancing the terms that are linear in deflection with the product of R_3 and a term that scales with deflection cubed gives $\langle y_{\mathrm{defl}}\rangle \sim R_3^{-1/2}$. The slight increase in $\langle y_{\mathrm{defl}}\rangle$ between $R_3 = 10^{2.5}$ and 10^3 when $R = 10^1$ (light blue line with upward-pointing triangle) and $R = 10^{1.5}$ (dark red line with right-pointing triangle) arises because for $R_3 = 10^{2.5}$ the discretization size of the membrane is $m = 120$ whereas for $R_3 = 10^3$ it is $m = 40$.

In Fig. 4 we saw that the motions do not change considerably with R_3 (apart from their amplitudes) except in the narrow transition region shown in the inset. We also find that the motions do not depend much on T_0 except close to the critical value of T_0 below which the flat state is unstable. In Table 2 we show membrane snapshots in the full four-dimensional parameter space R_1–T_0–R_3–R, collected into four subpanels, each with a particular value of T_0 and R_3 (labeled at top and left, respectively), and with a range of values of R_1 and R within each subpanel. There is more variation within a given subpanel than between corresponding points in different subpanels, indicating that R and R_1 have a stronger effect on the dynamics than T_0 and R_3. The white background and flat lines at $R_1 = 10^{-1}$ and $R \geq 10^0$ when $T_0 = 10^{-1}$ (top row) indicate stable membranes, so the deflection there is zero. From this comparison we see that, as in the previous figure, the deflections decrease with increasing R_3 (values in color bars at right) but often the snapshot shapes do not change much, at the same (R_1, R) values. Some membranes with moderate values of R_1 (10^0 and 10^1) have more prominent differences as R_3 is changed, sometimes by altering the location of a transition between different types of dynamics. Decreasing the value of T_0 can cause stable membranes to become unstable (e.g., at $R_1 = 10^{-1}$), but otherwise decreasing T_0 has a small effect, mainly to increase the deflection slightly at a given R_3. Below 10^{-2}, the T_0 term in the membrane equation [Eq. (4)] becomes insignificant, as noted in Mavroyiakoumou and Alben (2020).

In Fig. 6, we focus on the lower left subpanel of Table 2, but double the density of values of R_1 and R, and decrease the lower limit of R_1, to obtain a more comprehensive picture of the dynamics. The motions in Fig. 6 have the largest deflection amplitudes at the largest $R_1 = 10^2$. As mentioned in Mavroyiakoumou and Alben (2020), we hypothesize that at large R_1 membrane inertia allows the membrane to maintain its momentum for longer times against restoring fluid forces, and obtain larger deflections (with longer periods, as we will show) before reversing direction. The same has been observed for flutter with bending rigidity (Connell and Yue, 2007; Alben and Shelley, 2008). As R_1 decreases, the membrane deflection amplitudes progressively decrease until the motions become difficult to resolve numerically (for $R_1 \lesssim 10^{-1}$). In this region, we find chaotic membrane oscillations with very small amplitudes and high spatial frequencies. To obtain numerically-converged motions with respect to the spatial grid when $R_1 \leq 10^{-1}$ we use more discretization points. In the lower-left corner in Fig. 6, i.e., $(R_1, R) = (10^{-1.5}, 10^{-1})$, $(10^{-1.5}, 10^{-0.75})$, and $(10^{-1.25}, 10^{-1})$, snapshots are omitted because steady-state membrane motions were not obtained.

Table 2
Table of plots showing snapshots of large-amplitude membrane motions in R_1–R space for two values of stretching rigidity R_3 ($10^{1.5}$ in left column, 10^3 in right column) and two values of pretension T_0 (10^{-1} in top row, 10^{-2} in bottom row). Colors represent the time-averaged deflection defined by Eq. (11).

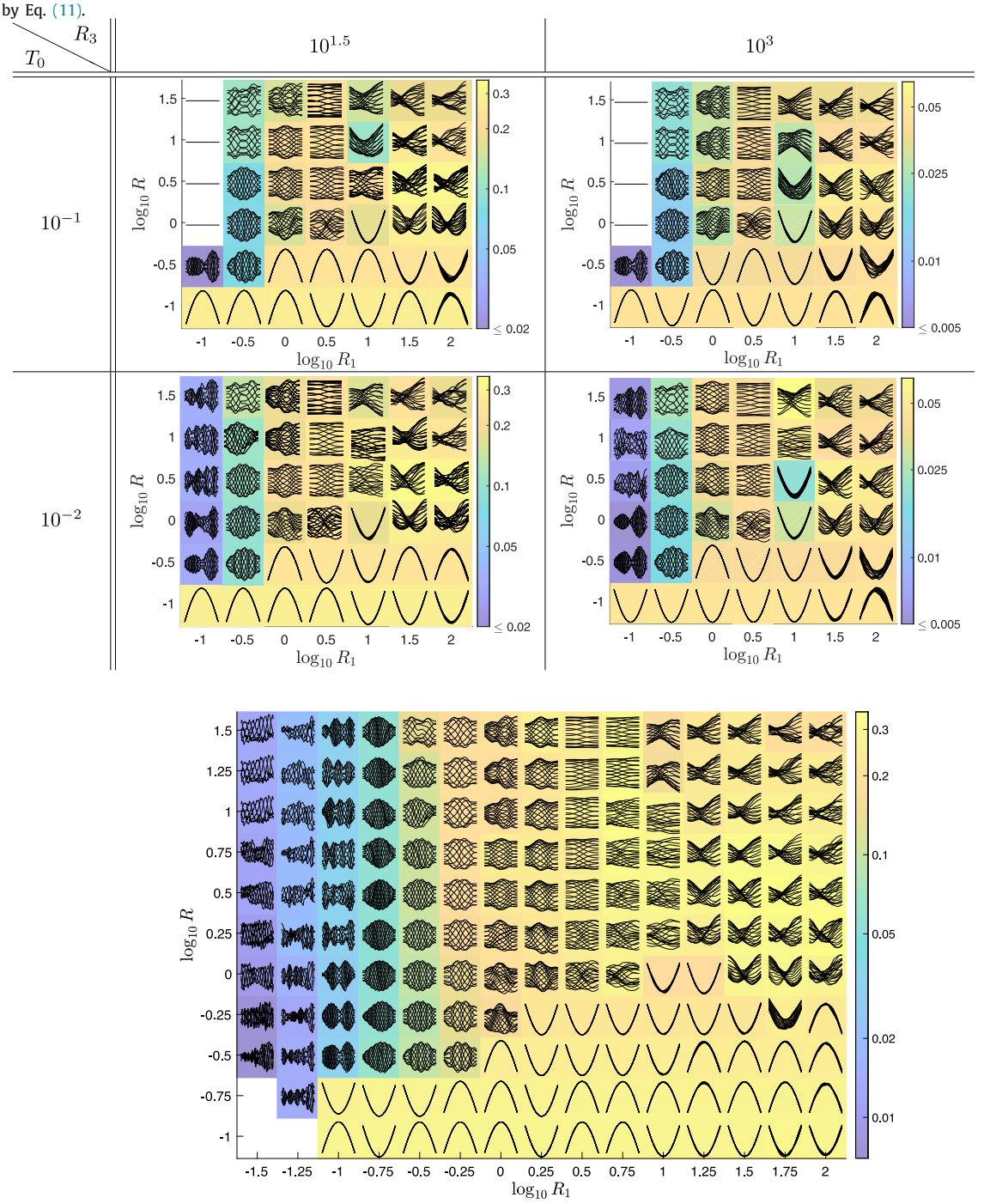

Fig. 6. (Inextensible rods) Membrane profiles in the large-amplitude steady-state regime, in R_1–R space for fixed $T_0 = 10^{-2}$ (dimensionless pretension) and $R_3 = 10^{1.5}$ (dimensionless stretching rigidity). The colored background represents the time-averaged deflection of the membranes defined by Eq. (11). (For interpretation of the references to color in this figure legend, the reader is referred to the web version of this article.)

Decreasing the membrane mass ratio (R_1) generally tends to introduce more oscillating states and fewer single-hump solutions for R values in the range $(10^{-0.75}, 10^{0.25})$. For large R_1 (heavy membranes) the maximum deflection of the

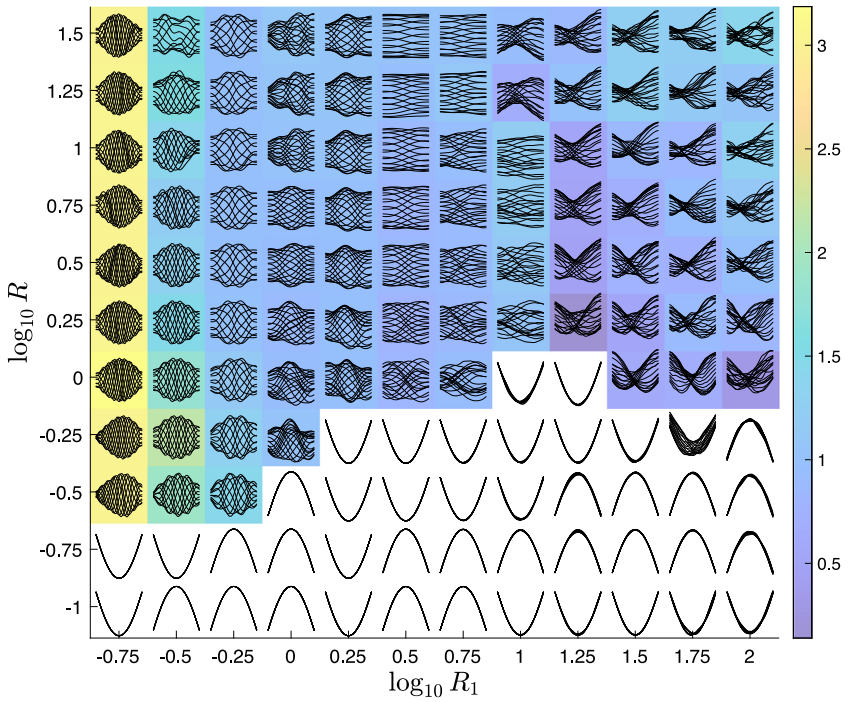

Fig. 7. (Inextensible rods) Colors represent the time-averaged number of zero-crossings (values in color bar at right) for membrane flutter in the R_1–R parameter space for fixed $T_0 = 10^{-2}$ and $R_3 = 10^{1.5}$. Note that R_1 is the dimensionless membrane mass, T_0 is the dimensionless pretension, and R_3 is the dimensionless stretching modulus. We also define R to be the length of the inextensible rods at either end of the membrane. The white background corresponds to membranes with no zero-crossings. At each (R_1, R) value the set of snapshots is normalized by the maximum deflection of the snapshots to show the motions more clearly. (For interpretation of the references to color in this figure legend, the reader is referred to the web version of this article.)

membrane occurs close to either the leading or trailing edge of the membrane. However, at $R_1 \in [10^{-0.75}, 10^{0.25}]$ the maximum membrane deflection seems to occur close to the midpoint of the membrane, with the deflection at the endpoints decreasing with decreasing R_1 in this region.

We now quantify the membrane shapes in terms of the time-averaged number of 'zero crossings'. Our definition is the number of crossings that a membrane makes with the line connecting its two endpoints, averaged over time—excluding the endpoints. This is one way to measure the 'waviness' of a shape that is not sinusoidal and whose wavelength is thus not well defined (Alben, 2015; Mavroyiakoumou and Alben, 2020). We first focus on moderate-to-large values of R_1 where the membranes have fewer zero-crossings (Fig. 7). Decreasing R_1 from the largest value (10^2), the average number of zero crossings changes non-monotonically. In most cases it decreases until about $R_1 = 10^{1.25}$ for $R \in [10^0, 10^1]$. Further decreases in R_1 give rise to more periodic motions with slightly larger numbers of zero-crossings. Independent of R_1, when T_0 and R_3 are fixed at 10^{-2} and $10^{1.5}$, respectively, and when the rods have a length of $\leq 10^{-0.75}$ then the membrane behaves similarly to the fixed–fixed case, where a single-hump solution is obtained. We use a white background for membranes with no zero-crossings (single hump solutions).

In Fig. 8 we present the zero-crossings in the small R_1 ($\leq 10^{-1}$) region, where higher spatial frequency components occur with decreasing R_1. The motions also become more irregular at the smallest R_1 values, where we increase the spatial grid density to resolve the fine undulations that appear on the membranes. On the right-hand side of Fig. 8 we show four panels with examples of sequences of membrane snapshots, equally spaced in time (with the thicker black line representing the membrane at the last time), to emphasize that even though the number of zero-crossings is a good measure of waviness it also misses some features of the shapes. For example, we see that the shape at $R_1 = 10^{-1.5}$ and $R = 10^0$ (bottom row of right-most column) has small undulatory features that are not reflected in the number of zero-crossings. In the small-R_1 region, the numbers of zero-crossings (shown by the colors) vary more rapidly compared to Fig. 7. In the lower-left corner, snapshots are omitted because steady-state membrane motions were not obtained.

To quantify the small undulatory features on the membranes, we calculate the time-averaged number of local extrema of deflection. In Fig. 9 we show that for fixed $R_3 = 10^{1.5}$, $T_0 = 10^{-2}$, and various fixed values of R, the time-averaged number of local extrema for small R_1 scales as R_1^{-1} approximately. At moderate-to-large values of R_1 (i.e., $[10^0, 10^2]$) and R small, the membranes tend to fore–aft symmetric, single-hump solutions and therefore the average number of extrema is one. For the oscillatory shapes that occur at larger values of R in the same region of R_1, the average number of local extrema is not large (i.e., between 1 and 5).

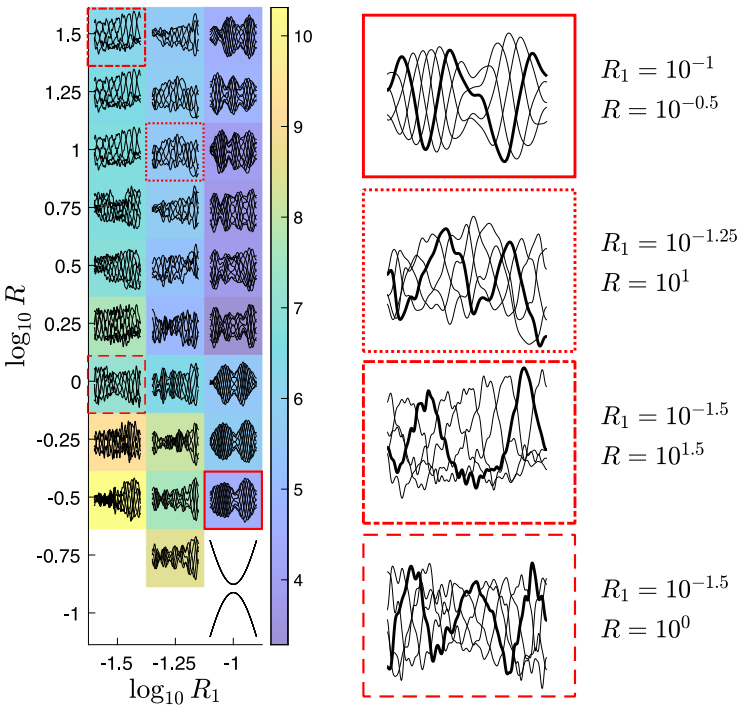

Fig. 8. (Inextensible rods) Colors represent the time-averaged number of zero-crossings (values in color bar at right) for membrane flutter in the R_1–R parameter space for fixed $T_0 = 10^{-2}$ and $R_3 = 10^{1.5}$ for light membranes ($R_1 \leq 10^{-1}$). Snapshots of these large-amplitude membrane motions are superposed to show the motions clearly in this region. (For interpretation of the references to color in this figure legend, the reader is referred to the web version of this article.)

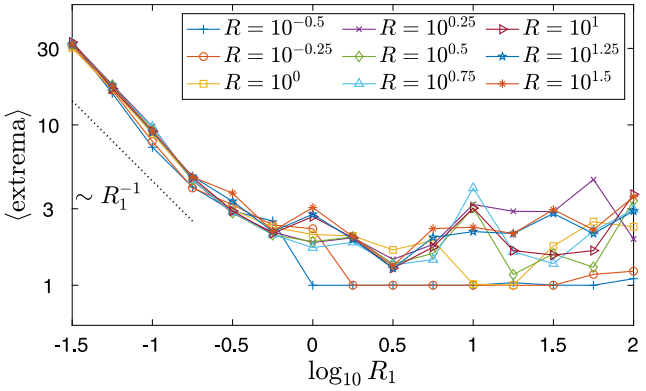

Fig. 9. (Inextensible rods) Time-averaged number of local extrema of the membranes versus the dimensionless mass density R_1 for various R and fixed $R_3 = 10^{1.5}$ and $T_0 = 10^{-2}$. The dotted black line at small R_1 indicates the scaling R_1^{-1}.

We have considered the amplitude of membrane deflection and its spatial frequency (in terms of zero crossings and numbers of extrema). The third main quantity we consider is the temporal period. We compute the power spectra of the time series of the membrane's midpoint, $y(0, t)$, using the fast Fourier transform. We identify the dominant frequency as that corresponding to the largest local maximum in the power spectrum (in a few cases excluding the peak closest to zero, which represents the time scale of the entire time series, and occurs because of the discontinuity in $y(0, t)$ at the beginning and end of the time series). The background color in Fig. 10 represents the dominant period, defined as the reciprocal of the dominant frequency, and is white for the steady single-hump solutions since the dominant period is undefined in the steady case. Similar to Figs. 6 and 8, in the lower-left corner, snapshots are omitted because steady-state membrane motions were not obtained.

We find different types of power spectra in different regions of R_1–R space, corresponding to the different motions illustrated in Fig. 10. At small R_1 ($\lesssim 10^{-1}$) the motions are more chaotic and there, the power spectra have a broad band

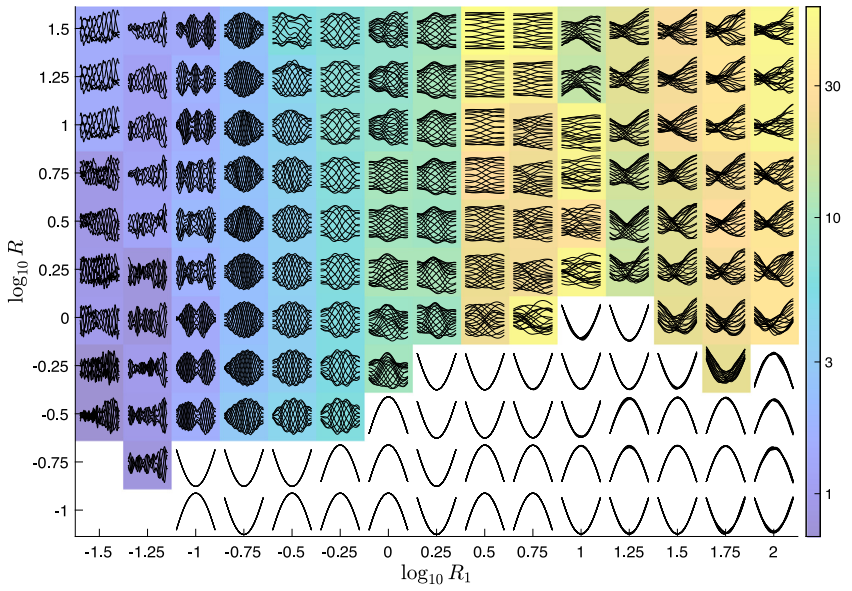

Fig. 10. (Inextensible rods) Colors represent the dominant periods (values in color bar at right) of large-amplitude motions for various R_1 and R, and fixed $T_0 = 10^{-2}$ and $R_3 = 10^{1.5}$. The data in the bottom-left corner are obtained for a shorter time and so we neglect the computational results for those values of R_1 and R. (For interpretation of the references to color in this figure legend, the reader is referred to the web version of this article.)

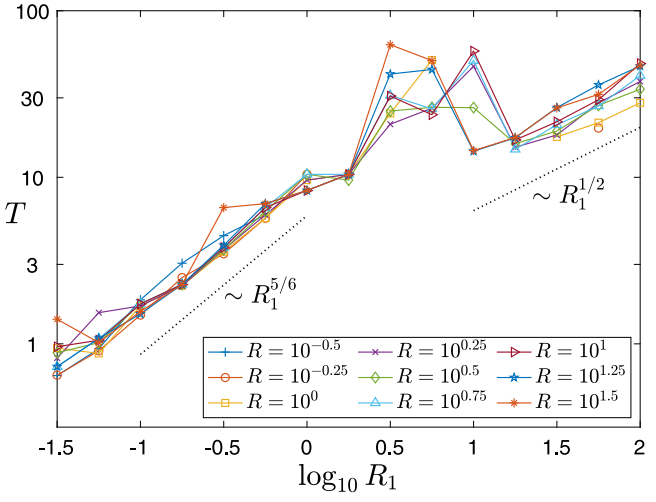

Fig. 11. Plots of the dominant period (T) versus mass density R_1 for various R and fixed $R_3 = 10^{1.5}$ and $T_0 = 10^{-2}$. The dotted black line at large R_1 shows the scaling $R_1^{1/2}$ and the dotted black line at small R_1 shows the scaling $R_1^{5/6}$.

of frequencies. At small-to-moderate values of R_1—between $10^{-0.75}$ and $10^{0.25}$—the motions are periodic and thus the power spectra have a discrete set of peaks. At moderate values of R_1—between $10^{0.5}$ and 10^{1}—the peak frequencies are decreased. Finally, for large values of R_1 ($\geq 10^{1.25}$) the motions become somewhat chaotic again (as at the smallest R_1), and with little dependence on R except at values greater than 10^{1}, where there is a slight increase in the dominant period. In Fig. 11 we show how the dominant period varies with R_1 for various fixed values of R. The trend at the largest R_1 is approximately $T \sim R_1^{1/2}$ (admittedly over a short range of R_1). This scaling arises when one approximates the normal component of the membrane equation [Eq. (4)] by its y-component, and chooses a characteristic time scale t_0 so that $R_1 \partial_{tt} y$ balances other terms that depend on y but not its time derivatives (i.e., the R_3 and T_0 terms and some of the fluid pressure terms). At large R_1, $R_1 \partial_{tt} y$ is comparable to the other terms when $R_1/T^2 \sim 1$ giving a typical period $T \sim R_1^{1/2}$. For some values of R, when $10^{0.25} < R_1 < 10^{1.25}$ and $R_1 > 10^{1.5}$, the period increases to > 30 as can be seen in Fig. 11. This range of moderate R_1 is a transition region, and at smaller R_1, (here, $10^{-1.5} \leq R_1 < 10^{0.25}$), another power law behavior is observed: $T \sim R_1^{5/6}$.

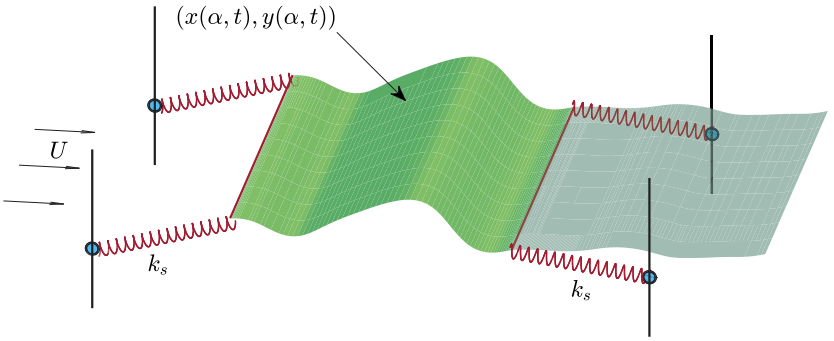

Fig. 12. Schematic diagram of a flexible membrane (green surface) at an instant in time. U is the oncoming flow velocity. There is also a vortex wake (light green surface) emanating from the membrane's trailing edge. The leading edge of the membrane with position $(x(-1,t), y(-1,t))$ is attached to springs (red coils) of spring constant k_s whose other ends are fixed at $(0,0)$ for all time. The membrane's trailing edge with position $(x(1,t), y(1,t))$ is attached to another spring whose other end is fixed at $(2,0)$. (For interpretation of the references to color in this figure legend, the reader is referred to the web version of this article.)

3.1. Hookean springs

The inextensible rods are a particular choice of tether motivated by the experiment of Kashy et al. (1997). In this section we briefly explore some alternative tethers involving Hookean springs. In the first case, we replace the inextensible rods at the ends of the membrane with springs of rest length zero that obey Hooke's law (Hooke, 1678). We illustrate schematically this alternative configuration in Fig. 12. The four prescribed dimensionless parameters are: membrane mass R_1, stretching rigidity R_3, pretension T_0, and spring stiffness k_s. We solve for the four endpoint unknowns ($x_{\pm1}$, $y_{\pm1}$) with four boundary conditions. At the membrane-spring contact, the tension forces must be equal in magnitude and direction to avoid infinite acceleration at the membrane ends, as for the rod tethers. Here the forces are equal in magnitude when:

$$k_s\sqrt{x_{-1}^2+y_{-1}^2} = T_{-1} \quad \text{and} \quad k_s\sqrt{(x_1-2)^2+y_1^2} = T_1. \tag{14}$$

Here $T_{\pm1}$ is the tension force at $\alpha = \pm1$ and $\sqrt{x_{-1}^2+y_{-1}^2}$ is the stretch of the spring (change in length from its rest length, zero). The directions of the tensions in the membrane and springs are equal if the slopes of the membrane and springs are equal:

$$\left.\frac{\partial_\alpha y}{\partial_\alpha x}\right|_{\alpha=-1} = \frac{y_{-1}-0}{x_{-1}-0} \quad \text{and} \quad \left.\frac{\partial_\alpha y}{\partial_\alpha x}\right|_{\alpha=1} = \frac{0-y_1}{2-x_1}. \tag{15}$$

When we simulate the spring-tethered membrane for various k_s, we find that for sufficiently large k_s, the membrane behaves like the fixed–fixed case, converging to a steady single-hump shape when the flat state is unstable. As we decrease k_s, the single hump solution continues until a threshold value of k_s (near unity) where the membrane develops a sharp spike at the trailing edge at early times and the simulations fail to converge beyond a short time. Unlike the inextensible-rod tethers, here the springs are too soft to ensure that the membrane remains under tension during the dynamics, and the membrane equation is ill-posed under compression (Triantafyllou and Howell, 1994).

3.2. Vertical Hookean springs

More interesting dynamics occur with springs in an alternative configuration, in which the springs are attached to massless rings that slide along vertical poles, shown in Fig. 13. This is the same as the free–free boundary condition except that the vertical motion is not free but instead resisted by springs. As in the free–free case, the vertical poles ensure that the membrane does not experience significant compression, and thus stable long-time oscillatory dynamics can occur. We will show that this boundary condition is equivalent to that of the inextensible-rod tethers in the limit of small deflections, so it provides an alternative way to understand the effect of the rods. Both the rods and vertical springs allow for a difference in resistance to transverse and in-plane motions, and hence allow for stable oscillatory large-amplitude flutter.

Here, by balancing the vertical forces on the rings, we obtain the mixed boundary conditions:

$$T_{-1}\left.\frac{\partial_\alpha y}{\partial_\alpha s}\right|_{\alpha=-1} - k_s y_{-1} = 0 \quad \text{and} \quad -T_1\left.\frac{\partial_\alpha y}{\partial_\alpha s}\right|_{\alpha=1} - k_s y_1 = 0. \tag{16}$$

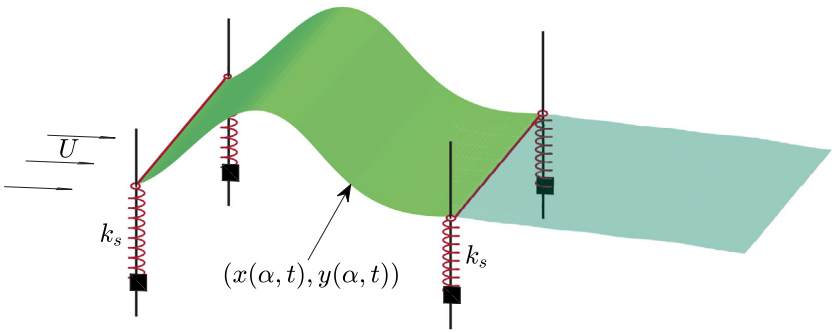

Fig. 13. Schematic diagram of a flexible membrane (green surface) at an instant in time. U is the oncoming flow velocity. There is also a vortex wake (light green surface) emanating from the membrane's trailing edge. The leading edge of the membrane with position $(0, y(-1, t))$ is attached to vertical springs (red coils) of spring constant k_s whose other end is fixed at (0,0) for all time. The membrane's trailing edge with position $(2, y(1, t))$ is attached to another vertical spring whose other end is fixed at $(2, 0)$. (For interpretation of the references to color in this figure legend, the reader is referred to the web version of this article.)

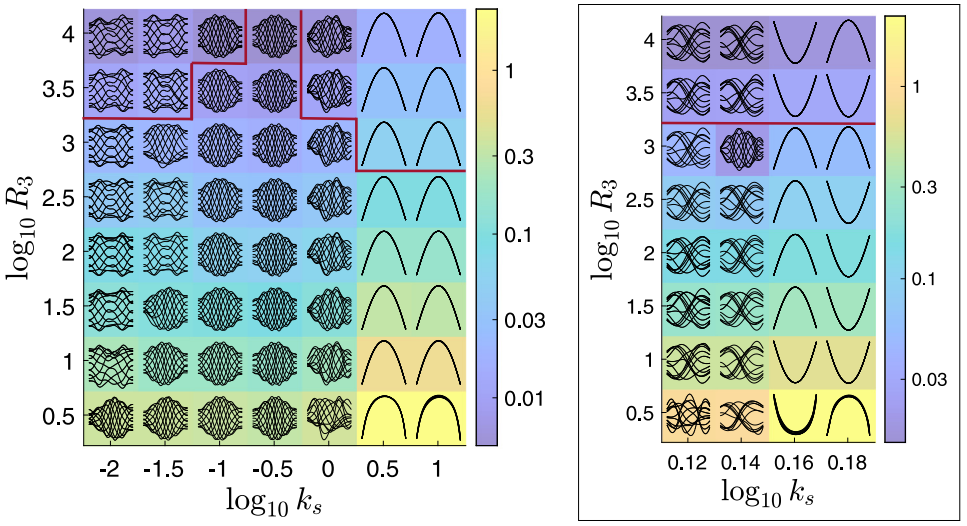

Fig. 14. (Vertical springs) Snapshots of large-amplitude membrane motions in k_s–R_3 space for fixed $T_0 = 10^{-2}$ and $R_1 = 10^{-0.5}$. Colors represent the time-averaged deflection of membranes defined by Eq. (11). Oscillatory ($k_s \leq 10^0$) and steady single-hump solutions ($k_s \geq 10^{0.5}$) are obtained. At each (k_s, R_3) value, the set of snapshots is scaled to fit within a colored rectangle at the (k_s, R_3) value and normalized by the maximum deflection of the snapshots to show the motions more clearly. The framed panel at right shows a finer grid between $k_s = 10^{0.12}$ and $10^{0.18}$, near the transitional k_s value. The red line separates membranes with $m = 40$ points (above) and $m = 80$ points (below). (For interpretation of the references to color in this figure legend, the reader is referred to the web version of this article.)

The free–free case corresponds to $k_s = 0$ (Mavroyiakoumou and Alben, 2020). The fixed–fixed case ($y(-1, t) = y(1, t) = 0$) occurs when $k_s \to \infty$. The remaining boundary conditions are $x_{-1} = 0$ and $x_1 = 2$, due to the poles.

In Fig. 14 we show membrane snapshots in the k_s–R_3 parameter space for fixed $T_0 = 10^{-2}$ and $R_1 = 10^{-0.5}$. The shapes are superposed on colors that represent the time-averaged deflections of the membranes [Eq. (11)]. As for the rod tethers, the stretching rigidity R_3 mainly affects the deflection of the membrane, not its shape. For $R_3 = 10^{0.5}$ and $k_s \in [10^{0.5}, 10^1]$ the deflections are so large that vortex shedding might not be confined to the trailing edge in reality, but we include these results to illustrate the model's behavior. The red line separates simulations with $m = 80$ points (below) and $m = 40$ (above); the smaller value is needed when $R_3 \geq 10^3$ to reach the steady-state regime. When $k_s \geq 10^{0.5}$ the membranes reach the single hump state, as in the fixed–fixed case, and for the rods with $R \leq 10^{-1}$ in Fig. 4.

There is a critical value of k_s at which the membrane transitions from the steady single-hump solutions to oscillatory motions. In the framed panel on the right-hand side of Fig. 14, we show the dynamics close to the transition. From $k_s = 10^0$ to $10^{0.12}$ the membrane shapes become less wavy. At $k_s = 10^{0.12}$ and $10^{0.14}$ they have only one "neck" in their deflection envelopes, apart from $(k_s, R_3) = (10^{0.12}, 10^{0.5})$ and $(10^{0.14}, 10^3)$.

4. Linearized membrane model

In this section we analyze the small-amplitude behavior of the system described in Section 2. We are able to present the small-amplitude motions of the membranes at a wide range of parameter values (membrane mass and pretension) by computing the eigenvalues and eigenmodes in detail, and after further simplifications, obtain asymptotic scaling laws. The modes resemble the large-amplitude motions qualitatively, and quantitatively in some cases. We consider small deflections $y(x,t)$ from the straight configuration, aligned with the flow. Since the membrane stretching factor is $\partial_\alpha s \approx 1+\partial_x y^2/2$, to linear order $\alpha \approx s \approx x$, all α-derivatives in Eq. (4) are x-derivatives, and $\zeta(\alpha,t) \approx \zeta(x,t) = x+iy(x,t)$. At linear order, the tangent and normal vectors are:

$$\hat{\mathbf{s}} \approx (1, \partial_x y)^\top, \quad \hat{\mathbf{n}} \approx (-\partial_x y, 1)^\top. \tag{17}$$

The linearized version of the membrane equation [Eq. (4)] is

$$R_1 \partial_{tt} y - T_0 \partial_{xx} y = -[p]. \tag{18}$$

When considering the linearized problem the term in the tension force $T(\alpha,t) = T_0 + R_3(\partial_\alpha s - 1)$ involving R_3 (dimensionless stretching rigidity) is neglected since it is of quadratic order, and so the linear dynamics are governed by the dimensionless membrane mass R_1 and the dimensionless pretension T_0.

The linearized conditions from Sections 2.1 and 3.2 are:

$$\text{Inextensible rods:} \quad x(-1,t) = 0,\ x(1,t) = 2,\ \partial_x y(-1,t) = \frac{1}{R} y(-1,t),\ \partial_x y(1,t) = -\frac{1}{R} y(1,t), \tag{19}$$

$$\text{Vertical Hookean springs:} \quad T_0 \partial_x y(-1,t) - k_s y(-1,t) = 0,\ -T_0 \partial_x y(1,t) - k_s y(1,t) = 0. \tag{20}$$

We note that the boundary conditions in Eqs. (19) are equivalent to Eqs. (20) with $1/R = k_s/T_0$. In Mavroyiakoumou and Alben (2020) the boundary conditions were (i) fixed–fixed: $y(\pm 1,t) = 0$, (ii) fixed–free: $y(-1,t) = 0$, $\partial_x y(1,t) = 0$, and (iii) free–free: $\partial_x y(\pm 1,t) = 0$.

The dynamics of the membrane are coupled to the fluid flow through the pressure jump term $[p](x,t)$. The linearized version of the pressure jump equation [Eq. (7)] is

$$\partial_t \gamma + \partial_x \gamma = \partial_x [p]. \tag{21}$$

The set of equations is closed by relating the vortex sheet strength $\gamma(x,t)$ back to the membrane position $y(x,t)$, through the kinematic condition [Eq. (6)], which in linearized form is:

$$\partial_t y(x,t) = -\partial_x y(x,t) + \frac{1}{2\pi} \int_{-1}^{1} \frac{v(x',t)}{\sqrt{1-x'^2}(x-x')}\, \mathrm{d}x' + \frac{1}{2\pi} \int_{1}^{\ell_w+1} \frac{\gamma(x',t)}{x-x'}\, \mathrm{d}x', \quad -1 < x < 1. \tag{22}$$

Here, we use that $\partial_t \overline{\zeta}(x,t) \approx -i\partial_t y$ and from Eq. (17), the normal velocity component is $\mathrm{Re}(\hat{\mathbf{n}} \partial_t \overline{\zeta}) \approx \partial_t y$. The general solution $\gamma(x,t)$ has inverse square-root singularities at $x = \pm 1$ and so we define $v(x,t)$, the bounded part of $\gamma(x,t)$, by $\gamma = v/\sqrt{1-x^2}$. The second integral in Eq. (22) represents the velocity induced by the vortex sheet wake, which extends downstream from the membrane on the interval $1 < x < \ell_w + 1$, $y = 0$. Therefore, the eigenvalue problem assumes a free vortex wake of a given fixed length ℓ_w, which we take to be large, 39 here, as in Mavroyiakoumou and Alben (2021). In that work, we found that the modes are essentially unchanged at larger values of ℓ_w. This long flat wake corresponds to starting with a deflection that is sufficiently small that we remain in the small-amplitude regime for large times.

The circulation in the wake,

$$\Gamma(x,t) = -\int_{x}^{\ell_w+1} \gamma(x',t)\, \mathrm{d}x', \tag{23}$$

is conserved along material points of the wake by Kelvin's circulation theorem. At linear order, the wake moves at the constant speed (unity) of the free stream; self-interaction is negligible.

At each time t, the total circulation in the wake, $\Gamma(1,t)$, is set by the Kutta condition, i.e.,

$$v(1,t) = 0. \tag{24}$$

Using the system of Eqs. (18), (21), (22), and (24) we solve for the following unknowns: the motion of the membrane and the strength of the vortex sheets along the membrane and in the wake.

For the linearized system, we may write solutions in the following form:

$$y(x,t) = Y(x)e^{i\sigma t}, \quad \gamma(x,t) = g(x)e^{i\sigma t}, \quad v(x,t) = V(x)e^{i\sigma t}, \quad \Gamma(1,t) = \Gamma_0 e^{i\sigma t}, \tag{25}$$

where Y, g, V, and Γ_0 are components of eigenmodes with complex eigenvalues $\sigma = \sigma_\mathrm{R} + i\sigma_\mathrm{I} \in \mathbb{C}$. The real parts of the eigenvalues are the angular frequencies and the imaginary parts are the temporal growth rates. If $\sigma_\mathrm{I} > 0$, small perturbations decay exponentially and the mode is stable, while if $\sigma_\mathrm{I} < 0$, small perturbations grow exponentially and the mode is unstable. If $\sigma_\mathrm{I} = 0$ the mode is neutrally stable. We wish to identify the region of R_1–T_0 space in which unstable eigenmodes exist, and when there are multiple unstable modes, identify the fastest growing mode.

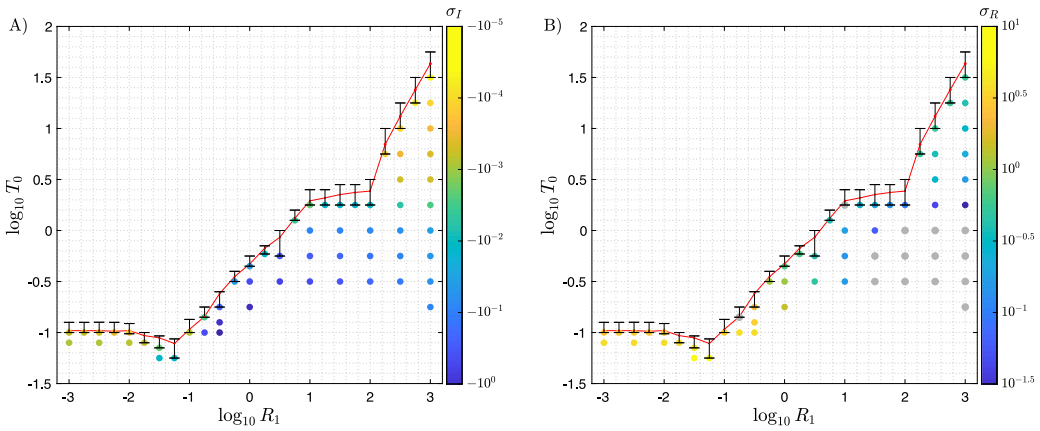

Fig. 15. (Vertical springs) The region in R_1–T_0 space in which membranes are unstable. The springs attached at the leading and trailing edges of the membrane have spring constant $k_s = 10^{-1}$. The red line and red dots indicate the position of the stability boundary computed using linear interpolation between σ_I of the smallest T_0 that gives a stable membrane and the σ_I of the largest T_0 that gives an unstable membrane (shown in the error bars). The color of the dots below the stability boundary labels: (A) The imaginary part of the eigenvalue (σ_I) corresponding to the most unstable modes. It represents the temporal growth rate. (B) The real part of the eigenvalues (σ_R) for the most unstable mode, representing the angular frequency. The gray dots correspond to modes that lose stability by divergence and have $\sigma_R \leq 10^{-9}$. (For interpretation of the references to color in this figure legend, the reader is referred to the web version of this article.)

Since Γ is conserved at material points of the free vortex sheet as they move downstream (at speed 1), and the material point at location $x \geq 1$ at time t was at location $x = 1$ at time $t - (x - 1)$ we can write

$$\Gamma(x,t) = \Gamma_0 e^{i\sigma(t-(x-1))} = \Gamma_0 e^{-i\sigma(x-1)} e^{i\sigma t}, \quad 1 < x < \ell_w + 1, \tag{26}$$

$$\gamma(x,t) = \partial_x \Gamma(x,t) = -i\sigma \Gamma_0 e^{-i\sigma(x-1)} e^{i\sigma t}, \quad 1 < x < \ell_w + 1, \tag{27}$$

using $\Gamma(1,t)$ from Eq. (25). Inserting the eigenmodes (25) into the governing Eqs. (18) and (22), yields

$$-\sigma^2 R_1 Y = T_0 \partial_{xx} Y - i\sigma \int_{-1}^{1} g \, \mathrm{d}x - g, \tag{28}$$

and

$$i\sigma Y = -\partial_x Y + \frac{1}{2\pi} \int_{-1}^{1} \frac{V(x')}{\sqrt{1-x'^2}(x-x')} \, \mathrm{d}x' - \frac{1}{2\pi} i\sigma \Gamma_0 \int_{1}^{\ell_w+1} \frac{e^{-i\sigma(x'-1)}}{x-x'} \, \mathrm{d}x', \quad -1 < x < 1, \tag{29}$$

respectively. Because σ appears in the exponential in the second integral in Eq. (29), this is a nonlinear eigenvalue problem. We solve the nonlinear eigenvalue problem iteratively by the method shown in the Appendix, the same as in Mavroyiakoumou and Alben (2021).

4.1. Eigenmode analysis of membranes attached to vertical Hookean springs

For the small-amplitude analysis we focus on membranes attached to vertical Hookean springs, equivalent to rods (shown by Eqs. (19) and (20) with $1/R = k_s/T_0$).

In Fig. 15 we plot the imaginary (Fig. 15A) and real parts (Fig. 15B) of the most unstable eigenvalues in the region of instability for membranes attached to springs with spring constant $k_s = 10^{-1}$ in R_1–T_0 space. The red line marks the boundary where the eigenvalues change from all $\sigma_I > 0$ (stable membranes) to at least one $\sigma_I < 0$ (unstable membranes). The stability boundary moves to larger pretension (T_0) values with increasing membrane mass (R_1), starting at $R_1 = 10^{-1.25}$. As R_1 decreases below $10^{-1.75}$ the critical pretension reaches a lower plateau. Below and to the right of the red line is the unstable region. The red dots that mark the stability boundary are computed by linear interpolation of σ_I between neighboring T_0 values (shown by the horizontal black bars) that bracket the boundary: all σ_I are positive at the larger of the T_0 values and above, but one σ_I is negative at the smaller of the T_0 values. The gray dots in Fig. 15B indicate negative σ_I and nearly zero σ_R ($\sigma_R \leq 10^{-9}$) for the most unstable eigenmode, which corresponds to divergence without flutter; they occur at $(R_1, T_0) = (10^{-0.75}, 10^{-0.85})$, $(10^1, 10^{0.25})$, and several cases with $R_1 \geq 10^{1.5}$ and $T_0 \leq 10^0$. The colored dots in Fig. 15B indicate a nonzero real part (value in color bar at right) for the most unstable eigenmode, corresponding to flutter and divergence.

In Fig. 16 we examine the variations in the most unstable eigenmodes in the same (R_1, T_0) space as Fig. 15, corresponding to the eigenvalues shown there. We also include our results from Mavroyiakoumou and Alben (2021, Figs. 5 and 13) for the stability boundary when both ends of the membrane are fixed (dotted blue line) and when both ends of

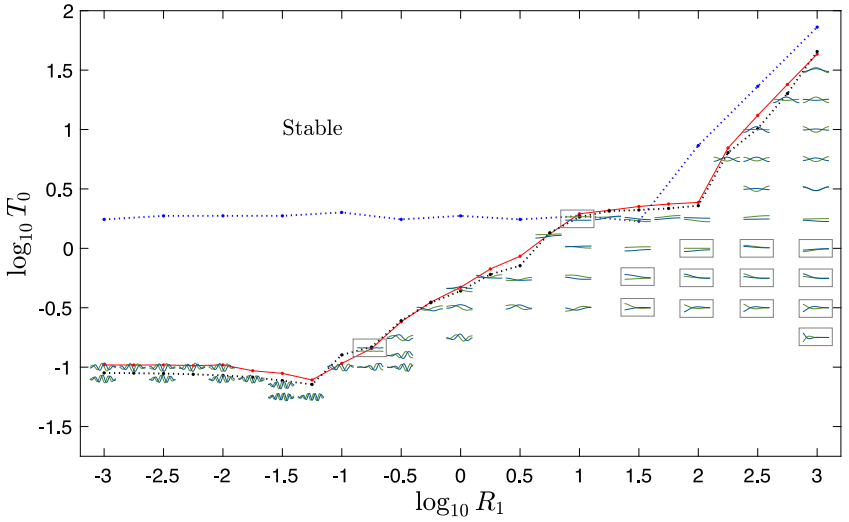

Fig. 16. (Vertical springs) The shapes $Y(x)$ of the most unstable eigenmode as a function of R_1 and T_0 with springs that have a spring stiffness of $k_s = 10^{-1}$. The real part of $Y(x)$ is shown in green and the imaginary part of $Y(x)$ is shown in blue. Each shape is scaled, both vertically and horizontally, to fit within the plot. Modes exhibiting a divergence instability have a gray rectangle outline. The shapes are superposed on the same stability boundary (red line) as in Fig. 15. The blue dotted line represents the stability boundary for fixed–fixed membranes and the black dotted line represents the stability boundary for free–free membranes from Mavroyiakoumou and Alben (2021). We include them here for comparison. (For interpretation of the references to color in this figure legend, the reader is referred to the web version of this article.)

the membrane are free (dotted black line). The real part of the eigenmode $Y(x)$ is shown in green and the imaginary part of $Y(x)$ is shown in blue. We place gray rectangles around the modes that lose stability by divergence. The shapes do not change noticeably for the wavier motions at $R_1 \in [10^{-3}, 10^{-2}]$. At these small R_1 values the deflection at the trailing edge is nearly zero. With R_1 increased to $(10^{-1}, 10^{-0.25})$, however, the maximum deflection occurs at the trailing edge of the membrane in most cases. Here and at some larger values of R_1, the mean slope of the membrane is nonzero. When $R_1 \in [10^{1.25}, 10^3]$ and $T_0 = 10^{0.25}$ the modes are nearly alike and their growth rates (σ_I, Fig. 15A) and angular frequencies (σ_R, Fig. 15B) are almost equal.

In the limit $R_1, T_0 \gg 1$, the fluid pressure is negligible and the linearized membrane equation reduces to the homogeneous wave equation

$$R_1 \partial_{tt} y - T_0 \partial_{xx} y = 0, \tag{30}$$

which after substituting the form of $y(x, t)$ from Eq. (25) becomes

$$-\sigma^2 R_1 Y - T_0 \partial_{xx} Y = 0. \tag{31}$$

The eigenmodes are combinations of $\cos(kx)$ and $\sin(kx)$, with $k = \pm\sigma\sqrt{R_1/T_0}$, satisfying the two boundary conditions in Eqs. (20). We find k by determining where the determinant of the matrix

$$\begin{pmatrix} -kT_0 \sin(-k) - k_s \cos(-k) & kT_0 \cos(-k) - k_s \sin(-k) \\ kT_0 \sin(k) - k_s \cos(k) & -kT_0 \cos(k) - k_s \sin(k) \end{pmatrix} \tag{32}$$

vanishes, which occurs if $k \sin(k) - (k_s/T_0)\cos(k) = 0$ or $k\cos(k) + (k_s/T_0)\sin(k) = 0$. The numerical solutions of these two nonlinear equations for $k_s = 10^{-1}$ and $T_0 = 10^1$ are:

$$k = 0.0998,\ 1.5771,\ 3.1448,\ 4.7145,\ 6.2848,\ 7.8553,\ 9.4258,\ 10.9965,\ 12.5672. \tag{33}$$

The eigenmodes are given by

$$Y(x) = \cos(k(x+1)) + \left(\frac{k_s}{T_0}\right)\frac{1}{k}\sin(k(x+1)), \tag{34}$$

with k from Eq. (33), for $-1 \le x \le 1$. Heavy membranes ($R_1 > 10^2$) with T_0 between $10^{0.25}$ and $T_{0C}(R_1)$ (i.e., the stability boundary) all lose stability with the third mode, $k = 3.1448$ in Eq. (34).

We now consider the analogous results when the Hookean spring constant is increased to $k_s = 10^0$. The stability boundary is shown as the red dots connected by red lines in Figs. 17A and 17B. As with $k_s = 10^{-1}$, the stability boundary moves to larger pretension (T_0) values with increasing membrane mass (R_1), starting at $R_1 = 10^2$. Now the critical pretension reaches a lower plateau at $R_1 = 10^0$ and below. The gray dots in Fig. 17B again indicate divergence without flutter (negative σ_I and nearly zero σ_R ($\le 10^{-9}$) for the most unstable eigenmode). We observe this for all $R_1 \le 10^0$

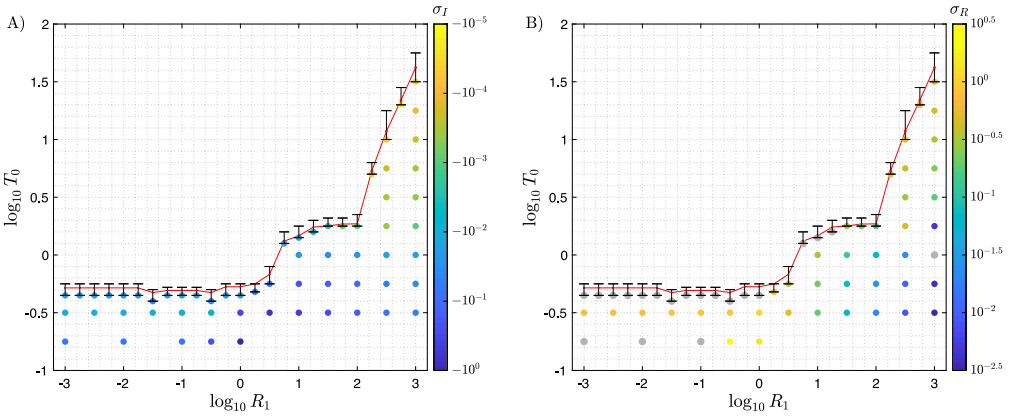

Fig. 17. (Vertical springs) Same as Fig. 15 but with $k_s = 10^0$.

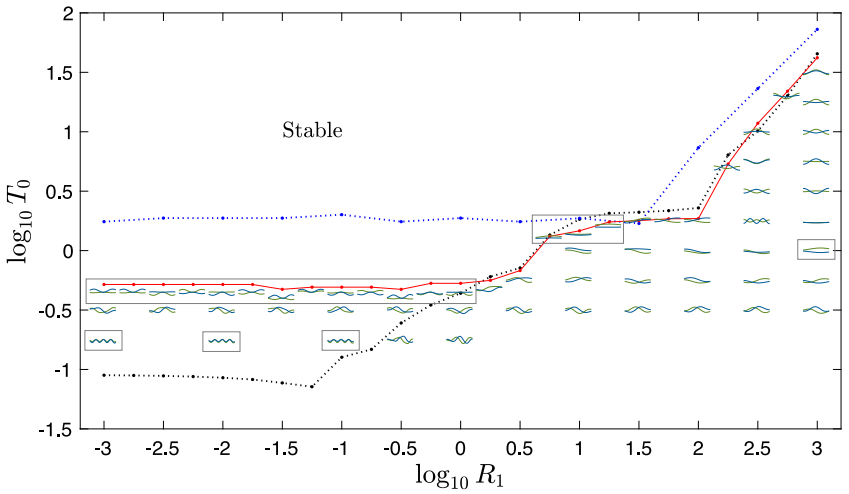

Fig. 18. (Vertical springs) Same as Fig. 16 but with $k_s = 10^0$.

and $R_1 \in [10^{0.75}, 10^{1.25}]$ close to the stability boundary, as well as for $(R_1, T_0) = (10^3, 10^0)$ and $R_1 \in [10^{-3}, 10^{-1}]$ with $T_0 = 10^{-0.75}$. Therefore, an increase in the spring stiffness not only changes the location and shape of the stability boundary but also leads to more instances of the divergence instability at smaller R_1 and fewer at larger R_1.

The corresponding eigenmodes are shown in Fig. 18. The critical pretension for $R_1 < 10^0$ is larger for $k_s = 10^0$ than for $k_s = 10^{-1}$ and lies almost midway between the stability boundary for fixed–fixed membranes ($k_s \to \infty$, blue dotted line) and for free–free membranes ($k_s = 0$, black dotted line). The mode shapes of light membranes $R_1 \leq 10^0$ close to the stability boundary have three extrema and are mostly symmetric. The shapes do not vary noticeably with R_1 at these R_1 values. The eigenvalues in Fig. 17 were also nearly constant in this region for fixed T_0. In general, as T_0 decreases the most unstable mode changes to a "wavier" profile at small R_1. However, there are exceptions: the membrane modes at $R_1 \geq 10^1$ and $T_0 = 10^0$ all have a similar shape (small but nonzero mean slope) but the associated eigenvalues vary more significantly there, as can be seen from Fig. 17.

Using $k_s = 10^0$ and $T_0 = 10^1$ we have that the determinant of Eq. (32) vanishes when

$$k = 0.3111,\ 1.6320,\ 3.1731,\ 4.7335,\ 6.2991,\ 7.8667,\ 9.4354,\ 11.0047,\ 12.5743. \tag{35}$$

When the mass density is between $10^{0.75}$ and 10^2 (especially close to the boundary), the membranes are similar in shape to those with $k_s = 10^{-1}$. The modes for heavy membranes ($R_1 > 10^2$), with T_0 between $10^{0.5}$ and $T_{0C}(R_1)$, all lose stability again with the third mode, $k = 3.1731$ in Eq. (34).

Increasing k_s further to 10^1 we approach the small-amplitude dynamics of a membrane whose edges are both fixed at zero deflection. In Fig. 19 the colored dots give the imaginary (Fig. 19A) and real parts (Fig. 19B) of the most unstable eigenvalues (with corresponding eigenmodes shown later, in Fig. 20). There are now many more cases of divergence without flutter (gray dots in Fig. 19B). At $R_1 > 10^2$ and $T_0 > 10^0$, divergence with flutter occurs (colored dots in Fig. 19B).

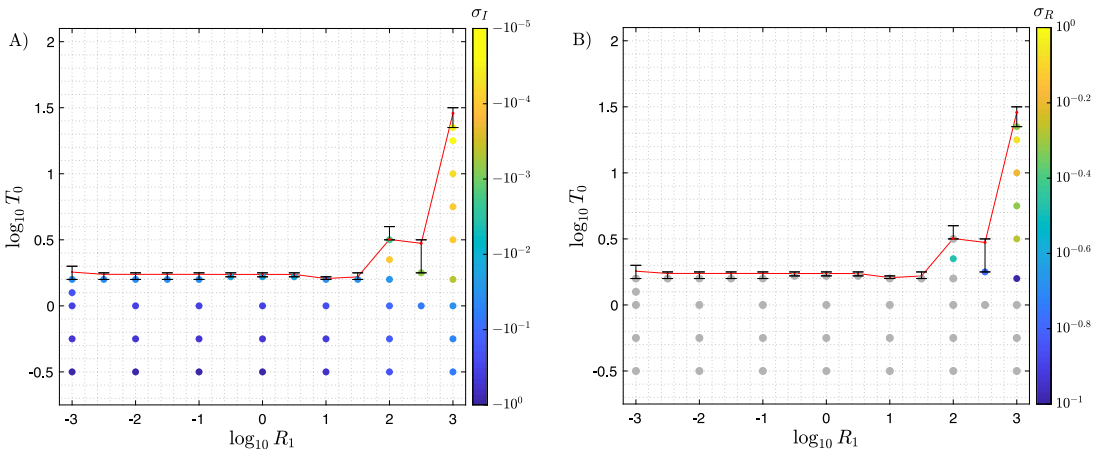

Fig. 19. (Vertical springs) Same as Fig. 15 but with $k_s = 10^1$.

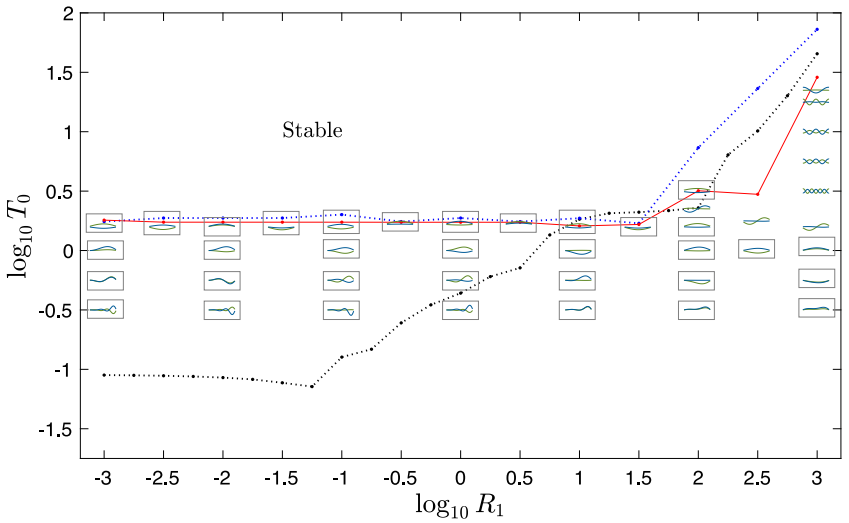

Fig. 20. (Vertical springs) Same as Fig. 16 but with $k_s = 10^1$.

In Fig. 20 we see that the critical pretension for $R_1 \leq 10^{1.5}$ is almost the same as the stability boundary for fixed–fixed membranes ($k_s \to \infty$, blue dotted line in Fig. 18). We place gray rectangles around the modes that lose stability by divergence. The shapes are also similar to the ones seen for a fixed–fixed membrane: For $R_1 < 10^2$ and T_0 just below T_{0C}, the unstable eigenmode is a single-hump shape that is nearly fore–aft symmetric. As the pretension is decreased further below T_{0C} (at $T_0 = 10^0$ and $R_1 < 10^{2.5}$) the divergent eigenmode becomes asymmetric, its maximum deflection point shifting towards the trailing edge. As the membrane mass (R_1) is increased to $10^{2.5}$, the maximum camber point moves towards the midchord and the membrane shape becomes almost fore–aft symmetric. At a smaller T_0 ($10^{-0.25}$) the membranes still lose stability by divergence but there is now an inflection point approximately at the membrane's midchord, with the maximum point on the membrane being closer to the aft part. Even though the membrane mode shapes generally look very similar to the fixed–fixed membranes in Mavroyiakoumou and Alben (2021, Fig. 5) when $k_s = 10^1$, this is not the case for $R_1 > 10^{2.5}$. The critical pretension in Fig. 20 starts to increase when $R_1 \gtrsim 10^2$ as opposed to a smaller mass, i.e., $R_1 \gtrsim 10^{1.5}$ for fixed–fixed membranes, and the mode shapes there are also very different. As for the other k_s values, here we use $k_s = 10^1$ and for a fixed value of T_0 determine the value of k such that the determinant of Eq. (32) is equal to zero. In Fig. 20 the first membrane that becomes unstable just below the stability boundary (at $T_0 = 10^{1.35}$) is approximately the third sinusoidal mode ($k = 3.28$). At $T_0 = 10^1$ and $10^{0.5}$ the most unstable modes are approximately the fifth and seventh sinusoidal modes ($k = 6.44$ and 9.74, respectively). The trend of odd-numbered modes does not continue when $T_0 < 10^{0.5}$.

To summarize, we have found that the stability boundary has an upward slope for large R_1, whereas for small-to-moderate R_1 values, the critical T_0 is smaller. At small R_1 the critical pretension for instability reaches a plateau value

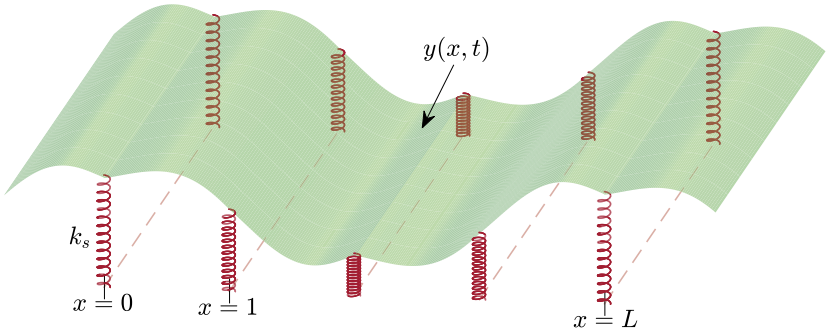

Fig. 21. Schematic diagram of a section of an infinite, flexible membrane (green surface) at an instant in time. Here L is the x-period of the membrane, $y(x,t)$ is the membrane deflection and the red springs of stiffness k_s are spaced one unit apart. The distance between springs is smaller than the membrane's period ($L > 1$, $L \in \mathbb{N}$). (For interpretation of the references to color in this figure legend, the reader is referred to the web version of this article.)

that depends on the spring stiffness. When R_1 and T_0 are dominant over fluid pressure forces, the membrane eigenmodes tend to neutrally-stable sinusoidal functions. Increasing the spring stiffness k_s introduces more divergence instabilities, in agreement with the fixed–fixed case studied in Mavroyiakoumou and Alben (2021). In general, the most unstable modes become more wavy at smaller T_0 and small R_1. The nonlinear eigenvalue problem for the linearized membrane model has allowed us to extend results from the large-amplitude model in Section 3 to a wider range of R_1–T_0 space. Next, we study a more analytically tractable model—that of an infinite, periodic array of springs attached to an infinite membrane. This model allows us to compute solutions for a much wider range of parameters and obtain asymptotic scaling laws.

5. Periodic array of springs on an infinite membrane

We have seen that the eigenvalue problem for a membrane tethered with springs (or rods) interpolates between the fixed–fixed and free–free cases. The vortex sheet wake results in a nonlinear eigenvalue problem, requiring an iterative solver that is time-consuming, particularly at small T_0. We now consider a simplified model with spatially periodic solutions that will allow us to derive asymptotic scaling laws. We assume the membrane extends to infinity upstream and downstream, and is tethered by an infinite, periodic array of Hookean springs (with stiffness k_s). The horizontal spacing between the springs (unity) is analogous to the length of the finite membrane in the previous section. This problem is shown schematically in Fig. 21, where the green surface represents a section of the infinite membrane at an instant in time and the pairs of red coils on either side of the membrane span represent the springs. The membrane has period L. By taking L larger than the distance between the springs, the infinite periodic membrane may have different deflections at streamwise-adjacent spring locations, as occurs for the tethered finite membrane. As L increases, the membrane can assume a wider range of shapes, but the eigenvalue problem becomes more costly to solve. We choose $L = 4$ as a compromise between these competing considerations. The flow velocity is again uniform at infinity (far above and below the membrane). With an infinite membrane there is no free vortex wake, and the nonlinear eigenvalue problem is reduced to a quadratic eigenvalue problem, which has analytic solutions for the eigenvalues when $k_s = 0$. In Newman and Païdoussis (1991) a related approximate model was considered—an infinite membrane with two- and three-harmonic truncations that were used to approximate fixed–fixed boundary conditions. The system of governing equations is:

$$R_1 \partial_{tt} y - T_0 \partial_{xx} y = -[p] - k_s y(x,t)\delta_1(x), \tag{36}$$

$$\partial_t y + \partial_x y = \frac{1}{2\pi} \int_{-\infty}^{\infty} \frac{\gamma(x',t)}{x-x'}\, \mathrm{d}x', \tag{37}$$

$$\partial_t \gamma + \partial_x \gamma = \partial_x [p]. \tag{38}$$

In Eq. (36), $\delta_1(x)$ is a periodic Dirac delta function with period one, resulting in a spring force at each integer x, and proportional to $y(x,t)$, the vertical deflection there. We next write the membrane position, vortex sheet strength, and pressure jump across the membrane, each as a Fourier series with period L, and the periodic Dirac delta function as a Fourier series with period one:

$$y(x,t) = \sum_{k=-\infty}^{\infty} \hat{y}_k e^{i(2\pi k/L)x} e^{i\sigma t}, \quad \gamma(x,t) = \sum_{k=-\infty}^{\infty} \hat{\gamma}_k e^{i(2\pi k/L)x} e^{i\sigma t}, \tag{39}$$

$$[p](x,t) = \sum_{k=-\infty}^{\infty} \widehat{[p]}_k e^{i(2\pi k/L)x} e^{i\sigma t}, \quad \delta_1(x) = \sum_{k=-\infty}^{\infty} e^{i(2\pi k)x}, \tag{40}$$

respectively, where $\hat{y}_k$, $\hat{\gamma}_k$, $\widehat{[p]}_k$ are complex Fourier coefficients to be found.

Using Eqs. (39) and (40), the membrane equation [Eq. (36)] can be written as

$$\sum_{k=-\infty}^{\infty}\left(-\sigma^2 R_1\hat{y}_k + T_0\left(\frac{2\pi k}{L}\right)^2\hat{y}_k\right)e^{i(2\pi k/L)x} = -\sum_{k=-\infty}^{\infty}\widehat{[p]}_k e^{i(2\pi k/L)x} - k_s\sum_{k'=-\infty}^{\infty}\hat{y}_{k'}e^{i(2\pi k'/L)x}\sum_{k''=-\infty}^{\infty}e^{i(2\pi k'')x}, \tag{41}$$

having divided throughout by the common factor $e^{i\sigma t}$. Substituting Eqs. (39) into Eq. (37), we obtain

$$\sum_{k=-\infty}^{\infty}\left(i\sigma + i\frac{2\pi k}{L}\right)\hat{y}_k e^{i(2\pi k/L)x}e^{i\sigma t} = \sum_{k=-\infty}^{\infty} -\frac{i}{2}\operatorname{sgn}\left(\frac{2\pi k}{L}\right)\hat{\gamma}_k e^{i(2\pi k/L)x}e^{i\sigma t}, \tag{42}$$

which implies that

$$i\left(\sigma + \frac{2\pi k}{L}\right)\hat{y}_k = -\frac{i}{2}\operatorname{sgn}\left(\frac{2\pi k}{L}\right)\hat{\gamma}_k. \tag{43}$$

Similarly, if we substitute Eqs. (39) and (40) into Eq. (38), we get

$$i\left(\sigma + \frac{2\pi k}{L}\right)\hat{\gamma}_k = i\frac{2\pi k}{L}\widehat{[p]}_k. \tag{44}$$

Using Eqs. (43) and (44) in Eq. (37) and in Eq. (38), we obtain

$$\hat{\gamma}_k = -2\operatorname{sgn}(k)\left(\sigma + \frac{2\pi k}{L}\right)\hat{y}_k, \tag{45}$$

$$\widehat{[p]}_k = -\frac{L}{\pi|k|}\left(\sigma + \frac{2\pi k}{L}\right)^2\hat{y}_k, \tag{46}$$

respectively, where we use that $\operatorname{sgn}(2\pi k/L) = \operatorname{sgn}(k)$ and thus write Eq. (41), in terms of $\hat{y}_k$ only, as

$$\sum_{k=-\infty}^{\infty}\left(-\sigma^2 R_1 + T_0\left(\frac{2\pi k}{L}\right)^2\right)\hat{y}_k e^{i(2\pi k/L)x} = \sum_{k=-\infty}^{\infty}\frac{L}{\pi|k|}\left(\sigma + \frac{2\pi k}{L}\right)^2\hat{y}_k e^{i(2\pi k/L)x}$$
$$- k_s\sum_{k'=-\infty}^{\infty}\hat{y}_{k'}\left(\sum_{k''=-\infty}^{\infty}e^{i(2\pi(k''L+k')/L)x}\right). \tag{47}$$

We match coefficients of $e^{i(2\pi k/L)x}$ in Eq. (47) and obtain

$$\left(-R_1 - \frac{L}{\pi|k|}\right)\sigma^2\hat{y}_k - \frac{4k}{|k|}\sigma\hat{y}_k + \left(\frac{2\pi k}{L}\right)^2\left(T_0 - \frac{L}{\pi|k|}\right)\hat{y}_k + k_s\sum_{k'\equiv k \bmod L}\hat{y}_{k'} = 0, \tag{48}$$

for $k = -N, \ldots, -1, 1, \ldots, N$. The last sum in Eq. (48) includes those k' that are equal to k plus a multiple of L. If we make the truncation approximation that $\hat{y}_k = 0$ for $|k| > N$ then Eq. (48) is a system of $2N+1$ equations in $2N+1$ unknowns $\hat{y}_k$. In the derivation we assumed $k \neq 0$. From Eq. (43) we see that $\hat{y}_0 = 0$ (Hilbert transform of a constant is equal to zero). Therefore, we insert 0 for $\hat{y}_0$ in the system of equations and remove $\hat{y}_0$ from the unknowns, resulting in $2N$ equations in $2N$ unknowns.

Eq. (48) is a quadratic eigenvalue problem of the form

$$(A_2\sigma^2 + A_1\sigma + A_0)\hat{\mathbf{y}} = 0, \tag{49}$$

where A_2 and A_1 are diagonal matrices, A_0 is a rank-L matrix, and $\hat{\mathbf{y}}$ is the eigenvector of Fourier coefficients $\{\hat{y}_k, k = -N, \ldots, -1, 1, \ldots, N\}$. Using `polyeig` in MATLAB we solve for the eigenvalues σ and determine the fastest growing eigenmode, i.e., corresponding to the most negative σ_I.

In Fig. 22 we show the imaginary parts of the most unstable modes for the periodic membrane problem, over one period $0 \le x \le 4$, and thus with 4 subintervals between springs shown. In a few examples (at the corners) in panels A–D, we show the locations of the springs by small red lines. In many (but not all cases), the shapes seem to repeat 4 times. This is particularly true at larger k_s, where the springs are stronger and impose a period-1 component more strongly in the eigenmode. The real parts are similar and are omitted. Membranes that lose stability by divergence without flutter are again outlined with gray rectangles. We compute the relative error in the eigenvalues when $N = 2^8$ and 2^9:

$$\text{relative error} = \left|\frac{\sigma_{2^8} - \sigma_{2^9}}{\sigma_{2^9}}\right|. \tag{50}$$

The maximum relative error is small for the cases in Fig. 22: 0.0437 when $R_1 = 10^{-4}$ (Fig. 22A), 0.0269 when $R_1 = 10^{-1}$ (Fig. 22B), 0.00267 when $R_1 = 10^{0}$ (Fig. 22C), and 1.31×10^{-5} when $R_1 = 10^{4}$ (Fig. 22D).

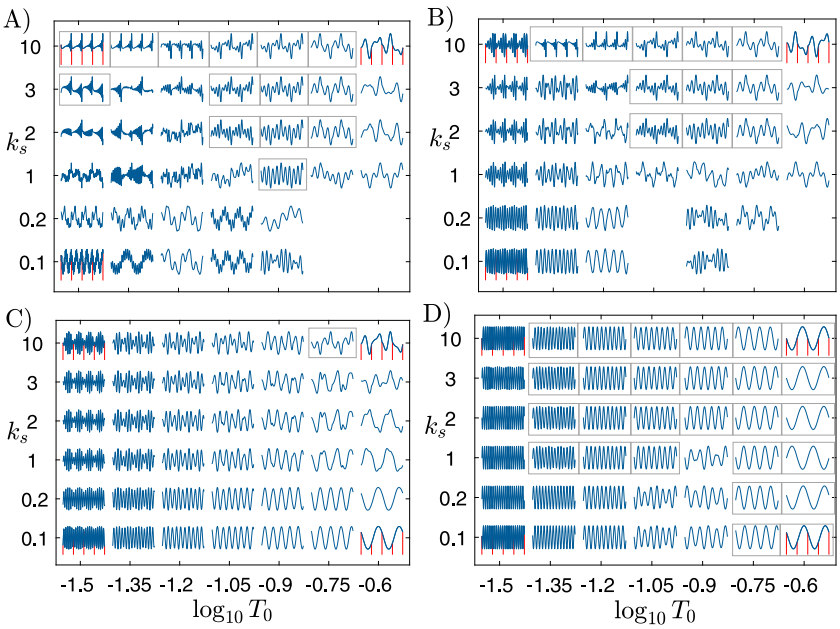

Fig. 22. Imaginary part of the most unstable eigenmode [Im($y(x)$)] in T_0–k_s parameter space for (A) $R_1 = 10^{-4}$, (B) $R_1 = 10^{-1}$, (C) $R_1 = 10^{0}$, and (D) $R_1 = 10^{4}$. Modes exhibiting a divergence instability with $\sigma_R \leq 10^{-9}$ have a gray rectangle outline. In all the panels, we use $N = 2^9$. (For interpretation of the references to color in this figure legend, the reader is referred to the web version of this article.)

The periodic membrane modes do not align precisely with those in the membrane-vortex-wake model due to the different membrane boundary conditions (periodic versus finite with a trailing vortex wake). However, there are many qualitative similarities. In both cases, the modes become sharper (or wavier) as we decrease T_0. At large R_1 the membranes are more sinusoidal with single bumps between the springs at large values of T_0 (in Fig. 22D for the periodic membrane). At small R_1 (Figs. 22A and 22B), the membranes are less sinusoidal and less symmetric. Another similarity at small R_1 is that increasing the spring stiffness k_s causes the maximum deflection point of the membrane to move downstream (to the right) with sharp peaks close to the spring locations (Figs. 22A and 22B as well as Fig. 16). Also true for both models is that the stability boundary shifts to lower T_0 at small R_1 and small k_s. As a result, at some locations in the lower right of panels A and B, membranes are omitted because all modes are stable, unlike at the corresponding locations in panels C and D (where R_1 is larger).

The membrane deflections at the springs increase when R_1 and T_0 increase relative to k_s. This can be seen by moving from left to right in some of the rows of Figs. 22A–C (i.e., increasing T_0 at fixed k_s), such as $k_s = 10^0$ in panel C. The same trend is seen moving from panel A to B to C to D, at the same location in each panel, i.e., increasing R_1 with k_s and T_0 fixed. A similar phenomenon was seen in the membrane-vortex-wake model.

In Fig. 23 we plot the imaginary parts of the most unstable eigenvalues as colored dots in the region of instability for membranes attached to a periodic array of springs with spring constants $k_s = 0$ (Fig. 23A), $k_s = 10^{-1}$ (Fig. 23B), $k_s = 10^0$ (Fig. 23C), and $k_s = 10^1$ (Fig. 23D). When $k_s = 0$, Eqs. (48) become decoupled scalar quadratic equations which can be solved analytically. The resulting σ_I are plotted in Fig. 23A. In Figs. 23B–D, $k_s \neq 0$, and we use the aforementioned MATLAB eigenvalue solver. With 2^9 modes, the results are resolved only in a small portion of Fig. 23A—a subset of the region within the red rectangle. The axis limits of panels B–D coincide with the red rectangle. Both the analytical results in panel A and the computed results in panels B–D are much easier to obtain than in the case of the membrane-vortex-wake model, so the data in all the panels of Fig. 23 are much more extensive than in Figs. 15, 17, and 19, a key advantage of the infinite-membrane model.

For this periodic problem, we see that the stability boundary at large R_1 plateaus, independent of the value of k_s, i.e., the critical pretension (T_0) is the same for all $R_1 \gtrsim 10^1$ instead of increasing with increasing mass as in the vortex-wake model (Figs. 15, 17, and 19). Although the stability boundaries differ at large R_1, here the vortex-wake model's eigenvalues are only slightly unstable [$\sigma_I = O(10^{-5})$] compared to neutrally stable ($\sigma_I = 0$) in the infinite membrane model.

We see that for smaller R_1 ($< 10^0$), the stability boundary in Fig. 23A is close to the diagonal line $T_0 = R_1$, and we will show this asymptotically in the next section. In panels B–D ($k_s \neq 0$), this line is no longer the stability boundary, but is instead the location of a sharp change in σ_I, shown by the sharp change in colors moving across this line, particularly in panel B and less so in C and D.

From the colors of the dots in all the panels we see that if we fix R_1 and decrease T_0, the growth rate σ_I becomes larger in magnitude (value in color bar at right). If we fix T_0 and increase R_1 above T_0, the growth rate σ_I becomes smaller in magnitude which implies slower growth of instabilities.

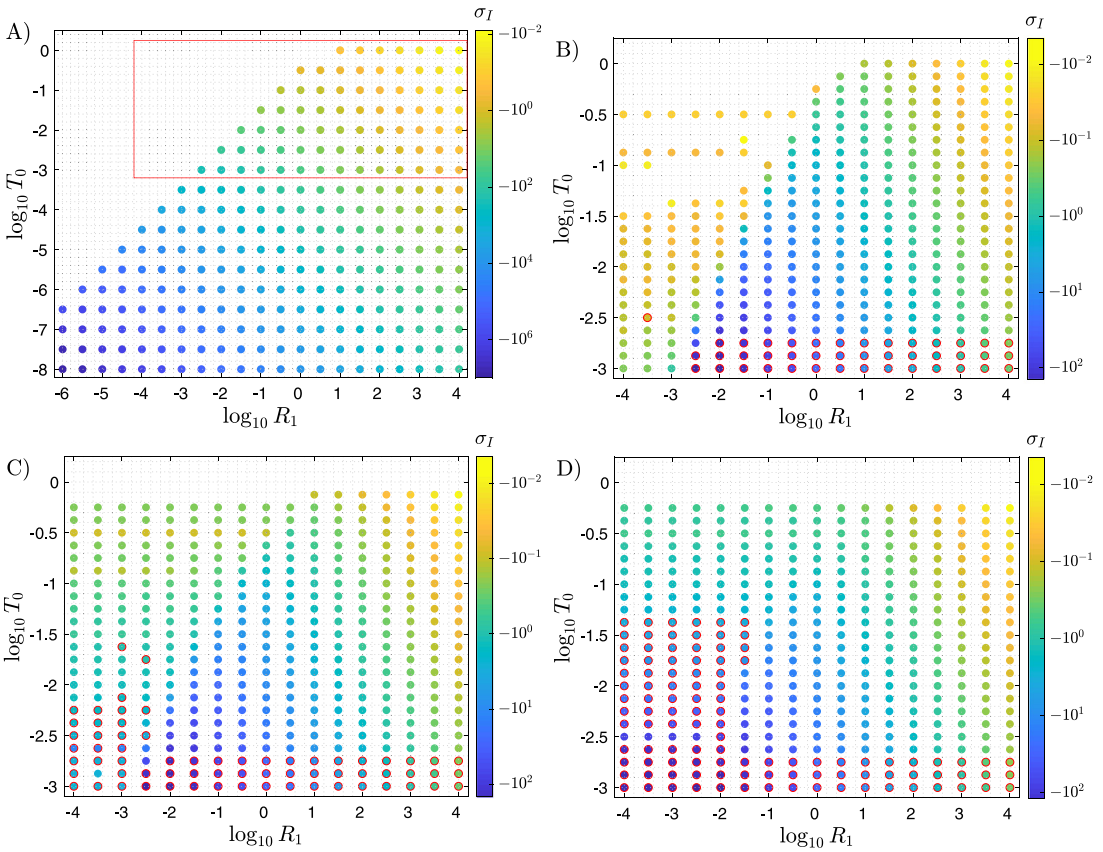

Fig. 23. (Infinite, periodic membrane) The region in R_1–T_0 space in which membranes are unstable. The color of the dots in the instability region labels the imaginary part of the eigenvalues (σ_I) corresponding to the most unstable modes. It represents the growth rate. The springs have stiffness values of: (A) $k_s = 0$ (analytical result), (B) $k_s = 10^{-1}$, (C) $k_s = 10^{0}$, and (D) $k_s = 10^{1}$. The numerical results shown in panels B–D are with $N = 2^9$. The red rectangle in panel A indicates the region we consider in panels B–D to facilitate comparison. The red outline on some of the colored dots indicates the cases where convergence with respect to N (as defined by Eq. (50)) was not obtained. (For interpretation of the references to color in this figure legend, the reader is referred to the web version of this article.)

In Fig. 23B, $k_s = 10^{-1}$ as in Fig. 15A for the membrane-vortex-wake model. There are two main points of qualitative agreement between the models in this case. One is that a lower plateau of the stability boundary occurs at small R_1; another is that the growth rates are much lower for $R_1 < T_0$. At this k_s value (10^{-1}) and at small R_1 and T_0 close to the stability boundary (e.g., at $T_0 = 10^{-0.5}$ and $10^{-0.875}$, for $R_1 \lesssim 10^{-2}$), there are also a few narrow bands of instability (lines of yellow dots) between stable regions, which was not observed in the membrane-vortex-wake model (Fig. 15A). Moving to Fig. 23C, k_s is increased to 10^0, and the stable regions in panel B surrounding the isolated bands become unstable in panel C, with larger growth rates than in the bands. Therefore, the stability boundary in panel C is almost at constant T_0 for all R_1, with a very small increase when $R_1 \geq 10^1$. An upward shift in the lower plateau is also seen in the vortex-wake model with the same increase in k_s, moving from Fig. 15A to Fig. 17A. Increasing k_s further to 10^1 (Fig. 23D) in the periodic membrane model these trends continue: the stability boundary is horizontal at $T_{0C} \approx 10^{-0.25}$ (a factor of ≈ 3 smaller than T_{0C} in the small-to-moderate R_1 region of Fig. 19), and the growth rates have increased further where $R_1 < T_0$. In Figs. 23B–D as T_0 decreases, $N = 2^9$ is eventually too small to resolve the most unstable eigenmodes. These cases are shown by red outlines around the colored dots, and become more prevalent as we move from panel B to C to D. These cases correspond to an eigenvalue relative error (as defined in Eq. (50))$> 3 \times 10^{-2}$ (chosen somewhat arbitrarily; other values give a similar classification of nonconvergence).

In Fig. 24 we plot the corresponding real parts of the eigenvalues for the most unstable modes. Increasing the spring stiffness k_s introduces more divergence modes (the gray dots, $\sigma_R \leq 10^{-9}$). Note that this also occurs in the vortex-wake model, Figs. 15, 17, and 19. σ_R varies more strongly with R_1 than with T_0. There is almost no variation with T_0 in Fig. 24A, and little variation in panels B–D—mainly when $T_0 > R_1$. Here, as T_0 decreases, σ_R increases but non-monotonically, particularly at the isolated bands of dots in panel B that become bands of non-monotonic change in σ_R in panels C and D, including changes between divergence (gray dots) and flutter and divergence (colored dots). Next we discuss more quantitatively how the real and imaginary parts of the eigenvalues depend on R_1 and T_0, including asymptotic scaling laws.

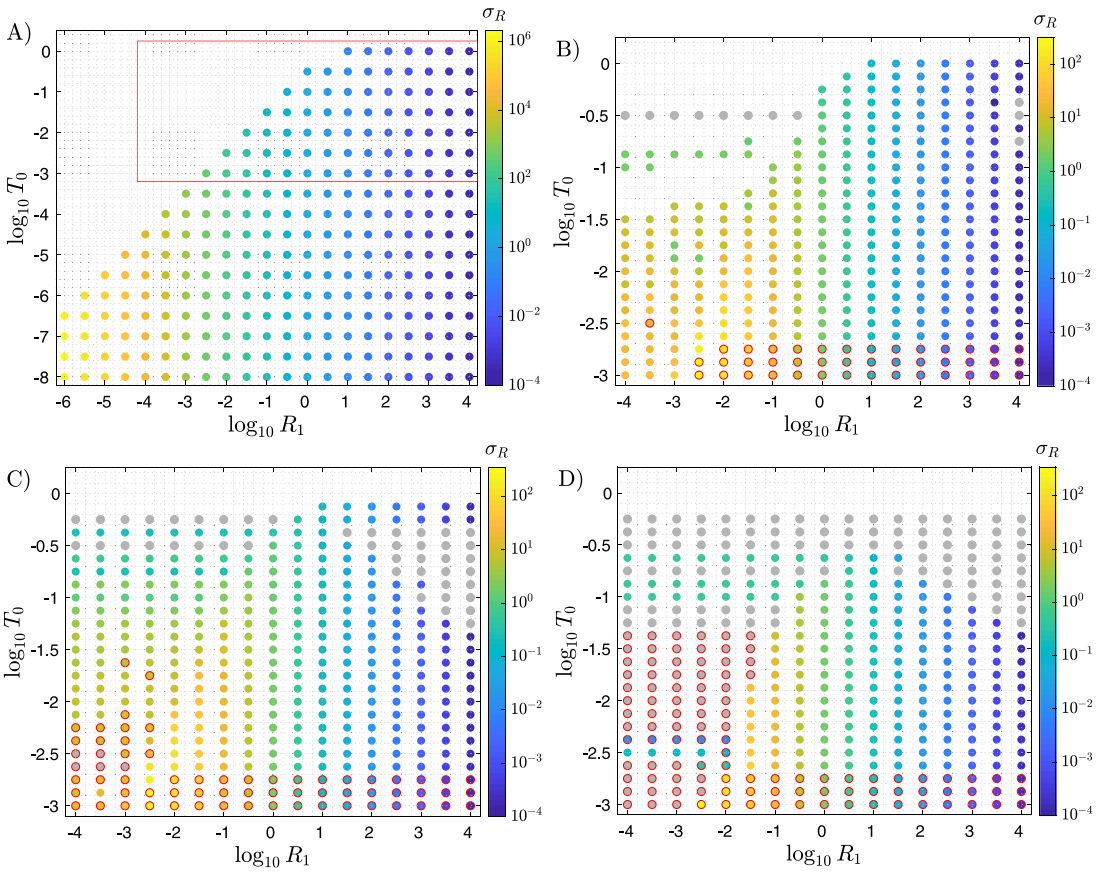

Fig. 24. (Infinite, periodic membrane) The region in R_1–T_0 space in which membranes are unstable. The color of the dots in the instability region labels the real part of the eigenvalues (σ_R) corresponding to the most unstable modes. It represents the angular frequency. The springs have stiffness values of: (A) $k_s = 0$ (analytical result), (B) $k_s = 10^{-1}$, (C) $k_s = 10^0$, and (D) $k_s = 10^1$. The numerical results shown in panels B–D are with $N = 2^9$. The gray dots correspond to modes that lose stability by divergence and have $\sigma_R \leq 10^{-9}$. The red rectangle in panel A indicates the region we consider in panels B–D to facilitate comparison. The red outline on some of the colored/gray dots indicates the cases where convergence with respect to N (as defined by Eq. (50)) was not obtained. (For interpretation of the references to color in this figure legend, the reader is referred to the web version of this article.)

5.1. Analytical results and scaling laws in the instability region

In this section we find analytically the eigenvalues and the corresponding eigenmodes (sinusoidal functions)—in the special case of $k_s = 0$. From these analytical solutions we derive asymptotic approximations for how the maximum growth rate, corresponding angular frequency, and dominant wave number depend on R_1 and T_0 when these parameters are small and large. We also study how the scaling laws behave when $k_s \neq 0$, where numerical solutions are required.

With $k_s = 0$ Eq. (48) reduces to

$$\left[\left(-R_1 - \frac{L}{\pi|k|}\right)\sigma^2 - \frac{4k}{|k|}\sigma + \left(\frac{2\pi k}{L}\right)^2\left(T_0 - \frac{L}{\pi|k|}\right)\right]\hat{y}_k = 0, \tag{51}$$

for $k = -\infty, \ldots, -1, 1, \ldots, \infty$. Solving Eq. (51) for σ, we obtain

$$\sigma = -\frac{2k}{|k|\,(R_1 + L/(\pi|k|))} \pm \sqrt{D_k}, \tag{52}$$

where

$$D_k := \frac{4}{(R_1 + L/(\pi|k|))^2}\left[1 + \left(R_1 + \frac{L}{\pi|k|}\right)\left(\frac{\pi k}{L}\right)^2\left(T_0 - \frac{L}{\pi|k|}\right)\right]. \tag{53}$$

The term in brackets can be written as $(L(-R_1 + T_0) + \pi R_1 T_0|k|)$ multiplied by a positive factor. Therefore D_k can be negative only for $T_0 < R_1$. When R_1 is small the R_1T_0 term is negligible, so the stability boundary follows $T_0 = R_1$ as shown in Fig. 23A.

Table 3
Summary of asymptotic scalings for the dominant wavenumber ($k_{\max}$), the real part of the eigenvalue (σ_R), and the imaginary part of the eigenvalue (σ_I) in the small- and large-R_1 and small-T_0 regimes, in the instability region.

Regimes	Quantities		
	$k_{\max}$	σ_R	σ_I
$R_1 \to \infty$ (fixed $T_0 \le T_{0C}$)	$\max\left(\frac{L}{2\pi T_0}, 1\right)$	$\frac{2}{R_1}$	$\max\left(\frac{1}{\sqrt{R_1 T_0}}, \frac{2\pi}{L\sqrt{R_1}}\sqrt{\frac{L}{\pi} - T_0}\right)$
$R_1 \to 0$ ($T_0 = cR_1$, $0 < c < 1$)	$\frac{LC}{4\pi T_0}$	$\frac{2C}{R_1(C+4c)}$	$\frac{\sqrt{C^3(4-4c-C)}}{2R_1(C+4c)\sqrt{c}}$
$T_0 \to 0$ (fixed R_1)	$\frac{L}{2\pi T_0}$	$\frac{2}{R_1}$	$\frac{1}{\sqrt{R_1 T_0}}$

In Eq. (52) there are two possible eigenvalues for each R_1 and T_0 combination (due to the square root) that correspond to a complex-conjugate pair. We can then find k for the most unstable mode by setting the derivative of Eq. (53) with respect to k to zero and solving for k:

$$k_{\max} = \pm\frac{L(R_1 - 5T_0) + L\sqrt{R_1^2 + 14R_1T_0 + T_0^2}}{4\pi R_1 T_0}. \tag{54}$$

Since the discriminant in Eq. (53) is symmetric about $k = 0$, we have a symmetric pair of $k_{\max}$ in Eq. (54). For the periodic membrane, $k_{\max}$ must be an integer, but Eq. (54) is not necessarily an integer. Restricting $k_{\max}$ to integer values, we find that it is given by one of the integers nearest to the value in Eq. (54).

With this model we are able to obtain asymptotic scaling laws in the instability region for a wide range of R_1 and T_0 values. Unstable membrane modes are realized when the argument of the radical in Eq. (52) is negative, i.e., $D_k < 0$ in Eq. (53). We will now present the asymptotic scaling laws for $k_{\max}$, σ_R, and σ_I in different limits within the instability region. As we do so, we will refer to the summary in Table 3. We study three asymptotic regimes that correspond to moving within the unstable region of Fig. 23A (or Fig. 24A) in three different directions. Moving rightward off to infinity, we have $R_1 \to \infty$ with fixed $T_0 \le T_{0C}$, the first row of Table 3. Moving diagonally downward and leftward, parallel to the stability boundary, we have $R_1 \to 0$ with $T_0 = cR_1$, for a fixed c between 0 and 1, the second row of Table 3. Moving vertically downward instead, we have $T_0 \to 0$ with fixed R_1, the third row of Table 3. Moving across each row, we give the asymptotic behavior of the three main quantities of interest. In the first column of Table 3, we give the asymptotic forms of $k_{\max}$ by taking the appropriate limits in Eq. (54). In the first and third rows, we obtain

$$k = k_{\max} \to \frac{L}{2\pi T_0}. \tag{55}$$

In the second row, setting $T_0 = cR_1$ and taking $R_1 \to 0$, we have

$$k = k_{\max} = \pm\frac{LC}{4\pi cR_1} = \pm\frac{LC}{4\pi T_0} \quad \text{where} \quad C = (1-5c) + \sqrt{1 + 14c + c^2}. \tag{56}$$

In Fig. 25 we plot the dominant wavenumber versus T_0 for various fixed values of R_1 (one per line) and for four values of spring stiffness: $k_s = 0$ (Fig. 25A), $k_s = 10^{-1}$ (Fig. 25B), $k_s = 10^0$ (Fig. 25C), and $k_s = 10^1$ (Fig. 25D). When $k_s = 0$, we have the analytical result in Eq. (54) (actually, the nonzero integer closest to it, as mentioned previously). We also still assume that the membrane has period $L = 4$, as in the $k_s \neq 0$ case discussed previously. In panel A, we find that the wavenumber does not vary significantly with R_1 except when $R_1 \ll 1$ and we are close to the stability boundary, i.e., $T_0 \approx R_1$ for small R_1. The lines in panel A with $R_1 \le 10^{-2}$ curve downwards towards a vertical asymptote as they approach the stability boundary, but $k_{\max}$ is bounded below by 1, the endpoint of each line. The dotted black line in Fig. 25A shows that the dominant wave number for various fixed R_1 values follows the scaling T_0^{-1}. Representative mode shapes at various (R_1, T_0) pairs are shown for $x \in [0, L]$, with the colors of the modes corresponding to the value of R_1. They are sinusoidal modes with wavelength that increases with T_0.

In panels B–D, $k_s \neq 0$, and the eigenmodes are found computationally. They are a superposition of multiple sinusoidal modes. For the most unstable mode we define the dominant wavenumber to be that of the sinusoidal component with the largest amplitude (the k for which $|\hat{y}_k|$ is largest [see Eq. (39)]). In Figs. 25B–D we find that at large R_1 ($\gtrsim 10^0$), where the spring force is relatively less significant, the lines scale as T_0^{-1} and do not vary significantly with R_1, similarly to the case without springs in panel A. At smaller R_1, the lines deviate greatly from this behavior, and do not seem to follow any specific power law. The data points outlined with black squares are cases that are not resolved (using the same definition as for the red circles in Figs. 23 and 24—when the eigenvalue relative error [Eq. (50)] $> 3 \times 10^{-2}$). These occur mostly at small T_0, when the dominant wavenumber $k_{\max}$ is very large, so good resolution would require a larger N than is feasible computationally. The deviations at small R_1 coincide with changes in the eigenmodes similar to those seen in Fig. 22 when R_1 and T_0 are small relative to k_s. In particular, the mode shapes are less sinusoidal and less symmetric than at

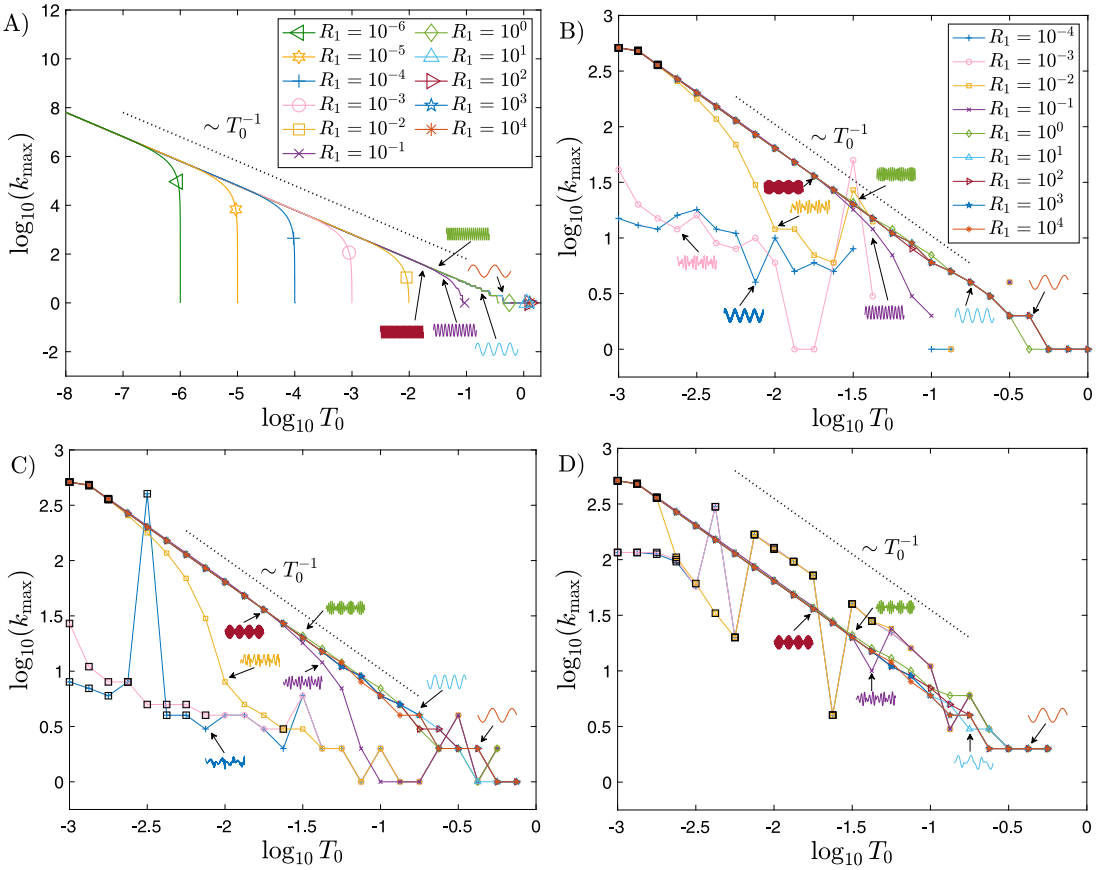

Fig. 25. (Infinite, periodic membrane) Plots showing the membrane's dominant wavenumber versus T_0 for various fixed R_1 values at four values of spring constants: (A) $k_s = 0$ (analytical results), (B) $k_s = 10^{-1}$, (C) $k_s = 10^{0}$, and (D) $k_s = 10^{1}$. We show typical examples of the imaginary part of the eigenmode shapes. The dotted black line shows the scaling T_0^{-1}.

large R_1. For example, as the spring stiffness k_s increases, moving from panel B to C to D, the envelopes of deflection for the green modes at $(R_1, T_0) = (10^0, 10^{-1.5})$ and the red modes at $(R_1, T_0) = (10^2, 10^{-1.75})$ are decreased near the springs at $x = 0, 1, \ldots, L = 4$. The light blue modes at $(R_1, T_0) = (10^1, 10^{-0.75})$ are sinusoidal in panels A–C but change to a non-sinusoidal shape at largest k_s (panel D), and the dominant wavenumber there is also decreased compared to the sinusoidal cases in panels A–C. The orange mode (at $(R_1, T_0) = (10^4, 10^{-0.375})$) has larger R_1 and therefore retains a sinusoidal shape even at the largest k_s value. Moving to much smaller R_1, such as the purple mode ($(R_1, T_0) = (10^{-1}, 10^{-1.375})$) we again have a transition from a sinusoidal shape at $k_s = 0$ to a shape that is less sinusoidal as k_s increases (from panels B to D) and less fore–aft symmetric, with peaks of deflection just upstream of the spring locations, unlike the more fore–aft symmetric red and green shapes at larger R_1.

We now present the real parts of the eigenvalues within the instability region, with three asymptotic behaviors given in the three rows of the second column of Table 3. For each row, we find the dominant behaviors of σ_R by inserting the values of $k_{\max}$ from the first column of that row into the first term on the right side of Eq. (52), which is σ_R. When we take the appropriate limits for each row (shown on the left side of Table 3), we obtain the expressions for σ_R in the second column of Table 3.

Fig. 26 plots the values of the real parts of the eigenvalues (σ_R) with respect to the membrane mass (R_1) for various fixed T_0 (one value per line) and for the same four spring stiffness constants as in Fig. 25, one per panel. As with Fig. 25A, the values in Fig. 26A, with $k_s = 0$, are obtained analytically through Eq. (52), and are obtained computationally for the remaining panels. Most of the data lie nearly on the straight line given by $2/R_1$, corresponding to the first and third rows in the second column of Table 3. For each $T_0 \leq 10^{-1}$, the corresponding line curves downward and becomes nearly vertical at the stability boundary. A vertical asymptote would occur if $k_{\max}$ could decrease to 0 (as in Eq. (54) when $R_1 \to T_0$), but it is bounded below by 1 (as in Fig. 25A), and consequently σ_R also has a positive lower bound at the stability boundary.

When k_s is increased from 0 to 10^{-1} we obtain different behaviors, shown in Fig. 26B. When $R_1 \gg 1$, the data follow the same $2/R_1$ behavior as in panel A for T_0 relatively large but below the stability boundary. At other (R_1, T_0) pairs, the springs cause different behaviors. Disconnected lines or points are observed (e.g., at $T_0 = 10^{-1.25}, 10^{-1}, 10^{-0.75}$) where

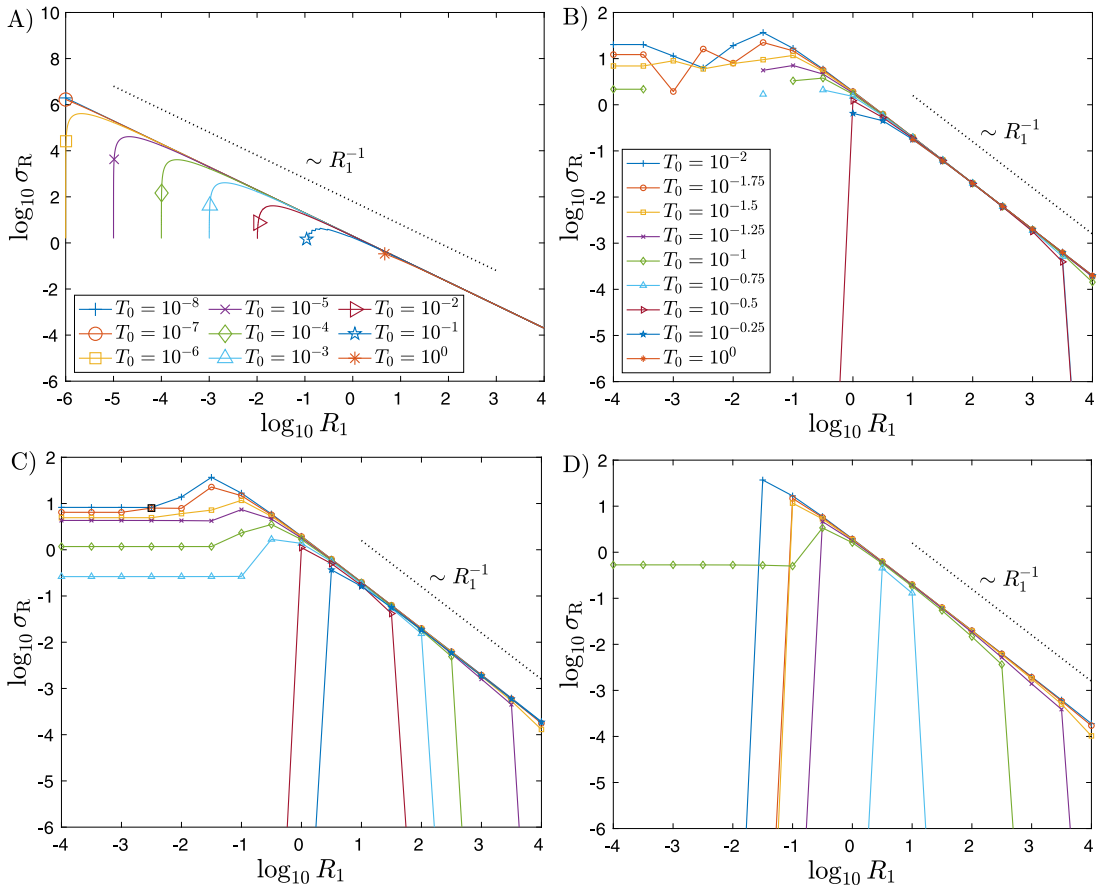

Fig. 26. (Infinite, periodic membrane) Plots showing the real parts of the eigenvalues for spring constants: (A) $k_s = 0$ (analytical result), (B) $k_s = 10^{-1}$, (C) $k_s = 10^{0}$, and (D) $k_s = 10^{1}$. Panels B–D share the same legend, and result from computations with $N = 2^9$. The dotted black line at moderate-to-large values of R_1 shows the scaling R_1^{-1}.

the membrane switches between being stable and unstable. These correspond to the isolated bands of unstable modes seen in Fig. 23B.

In Fig. 26 (panels B, C, and D), some membranes lose stability by divergence, shown by the sharp drop in some of the graphs to values below 10^{-6} (for example, $T_0 = 10^{-0.5}$ in panels B and C and $T_0 = 10^{-1.25}$ and $T_0 = 10^{-0.75}$ in panel D). The graphs continue to the left or right R_1 limits of the plots with values $\approx 10^{-12}$ (not visible), indicating instability by divergence throughout these regions. Divergence occurs for ranges of small and large R_1 that are generally more extensive at larger T_0 until the stability boundary is reached. When $T_0 = 10^{-0.25}$ and $10^{-0.5}$ in panel D all membranes lose stability by divergence. Therefore, the lines for these two cases do not appear in the panel. Another striking effect of $k_s \neq 0$ is the plateaus on the left sides of panels B–D, at small R_1. Here the values of σ_R drop to a plateau instead of a vertical asymptote as in panel A. The values of σ_R for each plateau decrease with increasing T_0 in most cases in panels B and C.

The small square with the black outline in panel C shows a case with an eigenvalue that is not converged. More of these cases occur in panel D where divergence occurs (below the lower limit of the panel, and so not shown).

Finally, we present the imaginary parts of the eigenvalues in the unstable region and investigate the same three asymptotic regimes as for the other two quantities in Table 3. For each regime, we derive the dominant behaviors of σ_I by substituting the k_{max} values shown in the first column of Table 3 in the second term on the right side of Eq. (52), which is $\pm i\sigma_I$ if $D_k < 0$, i.e., the mode is unstable.

In Fig. 27 we plot the imaginary parts of the eigenvalues (σ_I) versus the membrane mass (R_1) for various fixed values of T_0 and for the same spring stiffness constants, one per panel, as in Figs. 25 and 26. In Fig. 27A at large R_1 for fixed T_0, σ_I follows the $R_1^{-1/2}$ scaling shown by the dotted line. The lines are equispaced at large R_1, consistent with the scaling $T_0^{-1/2}$ for fixed R_1. Both behaviors are consistent with the asymptotic scaling law $\sigma_I \sim 1/\sqrt{R_1 T_0}$ at large R_1 or at small T_0, the first and third rows, respectively, of the third column of Table 3. As in Fig. 26A, each line curves downward to a vertical asymptote as it approaches the stability boundary at a certain R_1 value. The dashed line shows the R_1^{-1} scaling of σ_I when $T_0 = cR_1$, $0 < c < 1$ and $R_1 \to 0$, given analytically in the second row of the third column of Table 3.

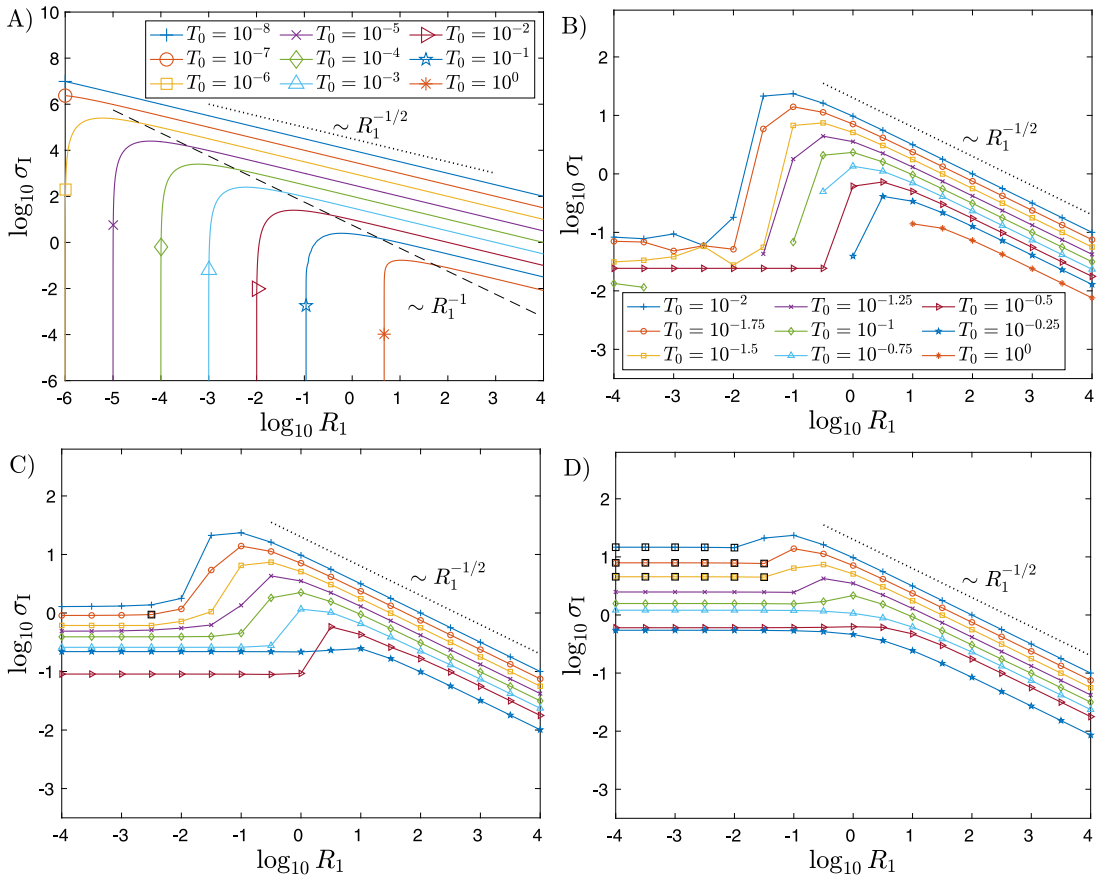

Fig. 27. (Infinite, periodic membrane) Plots showing the imaginary parts of the eigenvalues for spring constants: (A) $k_s = 0$ (analytical result), (B) $k_s = 10^{-1}$, (C) $k_s = 10^{0}$, and (D) $k_s = 10^{1}$. Panels B–D share the same legend, and for the numerical results shown we use $N = 2^9$. The dotted black line at moderate-to-large values of R_1 shows the scaling $R_1^{-1/2}$.

Panels B–D show the results with three nonzero k_s values, and have many similarities with the corresponding results for σ_R (Figs. 26B–D). For example, the lines end in panel B where the membrane switches between being stable and unstable. Another similarity, when $k_s \neq 0$, is that σ_I plateaus on the left sides of panels B–D, at small R_1. Here, when $T_0 \to R_1^-$ the lines of σ_I initially curve downward (but not towards a vertical asymptote as in Fig. 27A) and then tend to a constant value at small R_1 in most cases. These lines curve downward less sharply as k_s increases, and the region of downward curving disappears completely in some cases in panel D. Another qualitative similarity with Fig. 26 is that the growth rate $|\sigma_I|$ decreases with increasing T_0 in most cases. As previously, the small squares with the black outline in Figs. 27C and 27D correspond to (R_1, T_0) pairs where the eigenvalue is not converged with respect to N but we still include them here to distinguish them from stable membranes where a marker is omitted altogether.

There is no indication in Figs. 27B–D of a switch in behavior corresponding to the changes from divergence with flutter to divergence without flutter shown by the sudden drops in σ_R in Figs. 26B–D. In other words, the imaginary parts of the eigenvalues change smoothly despite the sharp changes in the real parts. The orange line with asterisks, $T_0 = 10^0$, is not present in Figs. 27C and 27D because the critical T_0 for instability drops below 10^0 as k_s increases to 10^0 and 10^1.

6. Summary and conclusions

In this work we have studied the flutter instability of thin membranes whose leading and trailing edges are attached to inextensible rods of length R and Hookean springs of stiffness constant k_s. We looked at different parts of the four-dimensional parameter spaces (R_1, R_3, T_0, R) and (R_1, R_3, T_0, k_s). We found that when membranes are attached to rods with small length R or to springs of moderate-to-large stiffness k_s, they exhibit large (but physically reasonable) deflections that converge to states of steady deflection with single humps that are almost fore–aft symmetric. When R is moderate-to-large and k_s small, we find a wide range of unsteady dynamics, somewhat similar to those seen in studies of flapping plates or flags (or fixed–free and free–free membranes in Mavroyiakoumou and Alben (2020)). In either of the two regimes, deflections scale as $R_3^{-1/2}$, when the stretching modulus R_3 is large. The large-amplitude dynamics depend most

strongly on the membrane mass density R_1 and less strongly on the pretension T_0. At the largest R_1 studied we find the smallest oscillation frequencies and largest membrane deflections corresponding to somewhat chaotic and asymmetrical membrane motions. Here the dominant time period scales as $R_1^{1/2}$. As R_1 decreases, the membrane motions become more periodic and symmetrical, and with larger spatial frequency components (sharper curvatures and more zero crossings). At $R_1 \lesssim 10^{-1.25}$ the motions become more chaotic again, with much finer spatial features that are difficult to resolve numerically and so a finer mesh on the membrane is required there. Our study shows that the boundary conditions (inextensible rods and vertical Hookean springs) allow for a smooth transition between types of membrane dynamics that were observed when both membrane ends are fixed at zero deflection or when one or both ends are free to move in the vertical direction.

To study the onset of membrane instability and small-amplitude membrane motions, we used a linearized model and a nonlinear eigenvalue solver – similar to the one in Mavroyiakoumou and Alben (2021). In this regime, the nonlinear R_3 term in Eq. (4) is negligible so we characterized the different types of motions with respect to the other two key dimensionless parameters – membrane mass and pretension. In the small-amplitude model we focused on the vertical Hookean springs, equivalent to inextensible rods via $1/R = k_s/T_0$. When membrane inertia and pretension dominate fluid pressure forces, the eigenmodes tend towards neutrally stable sinusoidal functions. As we increase k_s, we transition from membranes that resemble the free–free case to membranes that resemble the fixed–fixed case. There are roughly two regimes: small membrane density, where divergence occurs and the most unstable mode becomes more fore–aft asymmetric as one moves further into the instability region, and large membrane density, where flutter and divergence occur with approximately sinusoidal modes. In both regimes, the most unstable modes become wavier at smaller T_0 and small R_1, akin to the most unstable beam modes at smaller bending rigidity in Alben (2008). The stability boundaries with $k_s = 10^{-1}$ and 10^0 are very similar at large membrane densities, showing an upward slope for R_1. This upward slope for R_1 is also seen with $k_s = 10^1$ but it starts at a larger R_1.

To derive asymptotic scaling laws theoretically, we introduced a simplified model with spatially periodic solutions by assuming that the membrane extends to infinity upstream and downstream and is tethered by an infinite, periodic array of Hookean springs, all with stiffness k_s. This model corresponds to a standard eigenvalue problem, and is much faster to compute than the nonlinear eigenvalue problem of the membrane-vortex-wake model. We can thus study much wider ranges of the key parameters R_1, T_0, and k_s. When $k_s = 0$ we can compute asymptotic scaling laws for the real and imaginary parts of the eigenvalues, and the dominant wave number of the most unstable eigenmodes. We find that as R_1 increases from small to large, the dominant wave number scaling varies from R_1^{-1} to R_1^0 for the periodic membrane within the instability region. In the large amplitude simulations, the time-averaged number of extrema of deflection also changes from R_1^{-1} to R_1^0 scalings as R_1 increases from small to large. For the periodic membrane, the frequency σ_R scales as R_1^{-1} at both small and large R_1, while the large-amplitude dominant frequency transitions scales as $R_1^{-5/6}$ and $R_1^{-1/2}$, respectively. At small R_1, the large-amplitude results are mostly independent of T_0 within the instability region, while the periodic membrane results do depend on T_0. For the periodic membrane, we also considered the small-amplitude growth rate σ_I. At large R_1, it decays as $R_1^{-1/2}$ for a fixed T_0; at small R_1 and $T_0 = cR_1$ for $0 < c < 1$, it decays as R_1^{-1}. When k_s is increased to a nonzero value, both σ_R and σ_I plateau at small R_1.

There are qualitative similarities in the shapes of the stability boundaries for the periodic membrane and membrane-vortex-wake models. At small R_1, the stability boundaries have a plateau at a certain T_0 value, that decreases as k_s decreases. At large R_1, the periodic membrane has a flat stability boundary, while that with the vortex wake is upward sloping, corresponding to unstable modes at larger T_0, albeit with very slow growth rates. At all R_1, as k_s increases divergence modes become more common near the stability boundary in both models.

The membrane modes from the two models also share many features. For example, the mode shapes become wavier at smaller T_0 in both models. Additionally, by tracking the eigenmodes across the three parameter space of R_1, T_0, and k_s, we found that at larger R_1, the modes are more sinusoidal and fore–aft symmetric in both models. At small-to-moderate R_1, the modes are more asymmetric, with peak deflections shifted downstream.

Declaration of competing interest

The authors declare that they have no known competing financial interests or personal relationships that could have appeared to influence the work reported in this paper.

Acknowledgment

We acknowledge support from the National Science Foundation, USA Mathematical Biology program under Award No. DMS-1811889.

Appendix. Numerical method for determining the set of eigenvalues and eigenmodes for each membrane

We solve the nonlinear eigenvalue problem iteratively by the same method as in Mavroyiakoumou and Alben (2021) but we include a brief description here for completeness.

At each iteration, we have an approximation σ_0 to a given eigenvalue σ. We approximate the equations as a quadratic eigenvalue problem:

$$[\sigma^2 A_2 + \sigma A_1 + A_0(\sigma_0)]w = 0, \tag{A.1}$$

where the matrices A_2, A_1, A_0 are known from Eqs. (28), (29), and $g(x) = V(x)/\sqrt{1-x^2}$. The eigenvector consists w consists of: (a) values of the eigenmodes, defined as Y on the Chebyshev grid $\{x_j = \cos\theta_j,\ \theta_j = (j-1)\pi/m,\ j = 1, \ldots, m+1\}$ and (b) the scalar Γ_0. The term $A_0(\sigma)w$ includes the exponential integral involving σ in Eq. (29) as well as terms that are constant in σ. In the exponential integral, σ is fixed at σ_0, the value of σ from the previous iteration, resulting in the quadratic eigenvalue problem [Eq. (A.1)], which is solved using `polyeig` function in MATLAB. Eq. (A.1) has $2m+4$ eigenvalue solutions. As in Alben (2008), Mavroyiakoumou and Alben (2021), we define an error function as the difference between σ_0 and the eigenvalue (out of the $2m+4$ possibilities) closest to it. We also compute the derivatives of the error function (i.e., the Jacobian matrix) with respect to σ_R and σ_I using finite differences at the initial iterate, and update it at subsequent iterates using Broyden's approximate formula. The error function and Jacobian define the search direction (via Newton's formula) for the next iterate. With this approach we obtain superlinear convergence to a given eigenvalue. By using a wide range of initial guesses, we obtain convergence to various eigenvalues and corresponding eigenmodes. More details about the numerical method can be found in Mavroyiakoumou and Alben (2021).

References

Alben, S., 2008. The flapping-flag instability as a nonlinear eigenvalue problem. Phys. Fluids 20, 104106.

Alben, S., 2009. Simulating the dynamics of flexible bodies and vortex sheets. J. Comput. Phys. 228 (7), 2587–2603.

Alben, S., 2015. Flag flutter in inviscid channel flow. Phys. Fluids 27 (3), 033603.

Alben, S., Shelley, M.J., 2008. Flapping states of a flag in an inviscid fluid: bistability and the transition to chaos. Phys. Rev. Lett. 100 (7), 074301.

Arbós-Torrent, S., Ganapathisubramani, B., Palacios, R., 2013. Leading-and trailing-edge effects on the aeromechanics of membrane aerofoils. J. Fluids Struct. 38, 107–126.

Argentina, M., Mahadevan, L., 2005. Fluid-flow-induced flutter of a flag. Proc. Natl. Acad. Sci. 102 (6), 1829–1834.

Carrier, G.F., 1945. On the non-linear vibration problem of the elastic string. Quart. Appl. Math. 3 (2), 157–165.

Cheney, J.A., Konow, N., Bearnot, A., Swartz, S.M., 2015. A wrinkle in flight: the role of elastin fibres in the mechanical behaviour of bat wing membranes. J. R. Soc. Interface 12 (106), 20141286.

Colgate, S., 1996. Fundamentals of Sailing, Cruising, and Racing. WW Norton & Company, New York.

Connell, B.S.H., Yue, D.K.P., 2007. Flapping dynamics of a flag in a uniform stream. J. Fluid Mech. 581, 33–67.

Das, A., Breuer, K.S., Mathai, V., 2020a. Nonlinear modeling and characterization of ultrasoft silicone elastomers. Appl. Phys. Lett. 116 (20), 203702.

Das, A., Mathai, V., Breuer, K., 2020b. Deformation, forces, and flows associated with extremely compliant membrane disks. In: AIAA Scitech 2020 Forum. p. 1049.

Eloy, C., Lagrange, R., Souilliez, C., Schouveiler, L., 2008. Aeroelastic instability of cantilevered flexible plates in uniform flow. J. Fluid Mech. 611, 97–106. http://dx.doi.org/10.1017/S002211200800284X.

Eloy, C., Souilliez, C., Schouveiler, L., 2007. Flutter of a rectangular plate. J. Fluids Struct. 23 (6), 904–919.

Farlow, S.J., 1993. Partial Differential Equations for Scientists and Engineers. Courier Corporation, New York.

Gordnier, R.E., Attar, P.J., 2014. Impact of flexibility on the aerodynamics of an aspect ratio two membrane wing. J. Fluids Struct. 45, 138–152.

Graff, K.F., 1975. Wave Motion in Elastic Solids. Oxford University Press, Oxford, England.

Haruo, K., 1975. Flutter of hanging roofs and curved membrane roofs. Int. J. Solids Struct. 11 (4), 477–492.

Hooke, R., 1678. De potentia restitutiva, or of spring. Explaining the power of springing bodies. R. Soc. London 1–56.

Hu, H., Tamai, M., Murphy, J.T., 2008. Flexible-membrane airfoils at low Reynolds numbers. J. Aircr. 45 (5), 1767–1778.

Jaworski, J.W., 2012. Thrust and aerodynamic forces from an oscillating leading edge flap. AIAA J. 50 (12), 2928–2931.

Jaworski, J.W., Gordnier, R.E., 2012. High-order simulations of low Reynolds number membrane airfoils under prescribed motion. J. Fluids Struct. 31, 49–66.

Kashy, E., Johnson, D.A., McIntyre, J., Wolfe, S.L., 1997. Transverse standing waves in a string with free ends. Amer. J. Phys. 65 (4), 310–313.

Kimball, J., 2009. Physics of Sailing. CRC Press, Boca Raton, FL.

Knudson, W.C., 1991. Recent advances in the field of long span tension structures. Eng. Struct. 13 (2), 164–177.

Kornecki, A., Dowell, E.H., O'Brien, J., 1976. On the aeroelastic instability of two-dimensional panels in uniform incompressible flow. J. Sound Vib. 47, 163–178.

Le Maître, O., Huberson, S., De Cursi, E.S., 1999. Unsteady model of sail and flow interaction. J. Fluids Struct. 13 (1), 37–59.

Lian, Y., Shyy, W., 2005. Numerical simulations of membrane wing aerodynamics for micro air vehicle applications. J. Aircr. 42 (4), 865–873.

Manela, A., Weidenfeld, M., 2017. The 'hanging flag' problem: on the heaving motion of a thin filament in the limit of small flexural stiffness. J. Fluid Mech. 829, 190–213.

Mavroyiakoumou, C., Alben, S., 2020. Large-amplitude membrane flutter in inviscid flow. J. Fluid Mech. 891, A23. http://dx.doi.org/10.1017/jfm.2020.153.

Mavroyiakoumou, C., Alben, S., 2021. Eigenmode analysis of membrane stability in inviscid flow. Phys. Rev. Fluids 6, 043901. http://dx.doi.org/10.1103/PhysRevFluids.6.043901, URL: https://link.aps.org/doi/10.1103/PhysRevFluids.6.043901.

Michelin, S., Smith, S.G.L., Glover, B.J., 2008. Vortex shedding model of a flapping flag. J. Fluid Mech. 617, 1–10.

Narasimha, R., 1968. Non-linear vibration of an elastic string. J. Sound Vib. 8 (1), 134–146.

Nardini, M., Illingworth, S.J., Sandberg, R.D., 2018. Reduced-order modeling for fluid-structure interaction of membrane wings at low and moderate Reynolds numbers. In: 2018 AIAA Aerospace Sciences Meeting. p. 1544.

Nayfeh, A.H., Pai, P.F., 2008. Linear and Nonlinear Structural Mechanics. John Wiley & Sons, New York.

Newman, B.G., Low, H.T., 1984. Two-dimensional impervious sails: experimental results compared with theory. J. Fluid Mech. 144, 445–462.

Newman, B.G., Païdoussis, M.P., 1991. The stability of two-dimensional membranes in streaming flow. J. Fluids Struct. 5 (4), 443–454.

Pepper, W.B., Maydew, R.C., 1971. Aerodynamic decelerators-An engineering review. J. Aircr. 8 (1), 3–19.

Piquee, J., López, I., Breitsamter, C., Wüchner, R., Bletzinger, K.-U., 2018. Aerodynamic characteristics of an elasto-flexible membrane wing based on experimental and numerical investigations. In: 2018 Applied Aerodynamics Conference. p. 3338.

Rojratsirikul, P., Genc, M.S., Wang, Z., Gursul, I., 2011. Flow-induced vibrations of low aspect ratio rectangular membrane wings. J. Fluids Struct. 27 (8), 1296–1309.

Rojratsirikul, P., Wang, Z., Gursul, I., 2010. Effect of pre-strain and excess length on unsteady fluid–structure interactions of membrane airfoils. J. Fluids Struct. 26 (3), 359–376.
Schomberg, T., Gerland, F., Liese, F., Wünsch, O., Ruetten, M., 2018. Transition manipulation by the use of an electrorheologically driven membrane. In: 2018 Flow Control Conference. p. 3213.
Shelley, M.J., Vandenberghe, N., Zhang, J., 2005. Heavy flags undergo spontaneous oscillations in flowing water. Phys. Rev. Lett. 94 (9), 094302.
Shelley, M.J., Zhang, J., 2011. Flapping and bending bodies interacting with fluid flows. Annu. Rev. Fluid Mech. 43, 449–465.
Song, A., Tian, X., Israeli, E., Galvao, R., Bishop, K., Swartz, S., Breuer, K., 2008. Aeromechanics of membrane wings with implications for animal flight. AIAA J. 46 (8), 2096.
Stanford, B., Ifju, P., Albertani, R., Shyy, W., 2008. Fixed membrane wings for micro air vehicles: Experimental characterization, numerical modeling, and tailoring. Prog. Aerosp. Sci. 44 (4), 258–294.
Stein, K., Benney, R., Kalro, V., Tezduyar, T.E., Leonard, J., Accorsi, M., 2000. Parachute fluid–structure interactions: 3-D computation. Comput. Methods Appl. Mech. Engrg. 190 (3–4), 373–386.
Sun, X., Wang, S.-Z., Zhang, J.-Z., Ye, Z.-H., 2018. Bifurcations of vortex-induced vibrations of a fixed membrane wing at Re $\leq$ 1000. Nonlinear Dynam. 91 (4), 2097–2112.
Sunny, M.R., Sultan, C., Kapania, R.K., 2014. Optimal energy harvesting from a membrane attached to a tensegrity structure. AIAA J. 52 (2), 307–319.
Swartz, S.M., Groves, M.S., Kim, H.D., Walsh, W.R., 1996. Mechanical properties of bat wing membrane skin. J. Zool. 239 (2), 357–378.
Sygulski, R., 1996. Dynamic stability of pneumatic structures in wind: theory and experiment. J. Fluids Struct. 10 (8), 945–963.
Sygulski, R., 1997. Numerical analysis of membrane stability in air flow. J. Sound Vib. 201 (3), 281–292.
Sygulski, R., 2007. Stability of membrane in low subsonic flow. Inter. J. Non-Lin. Mech. 42 (1), 196–202.
Taneda, S., 1968. Waving motions of flags. J. Phys. Soc. Japan 24, 392–401.
Tang, L., Païdoussis, M.P., Jiang, J., 2009a. Cantilevered flexible plates in axial flow: energy transfer and the concept of flutter-mill. J. Sound Vib. 326 (1–2), 263–276.
Tang, L., Païdoussis, M.P., Jiang, J., 2009b. The dynamics of variants of two-dimensional cantilevered flexible plates in axial flow. J. Sound Vib. 323 (1–2), 214–231.
Tiomkin, S., Raveh, D.E., 2017. On the stability of two-dimensional membrane wings. J. Fluids Struct. 71, 143–163.
Tregidgo, L., Wang, Z., Gursul, I., 2013. Unsteady fluid–structure interactions of a pitching membrane wing. Aerosp. Sci. Technol. 28 (1), 79–90.
Triantafyllou, M.S., Howell, C.T., 1994. Dynamic response of cables under negative tension: an ill-posed problem. J. Sound Vib. 173 (4), 433–447.
Tzezana, G.A., Breuer, K.S., 2019. Thrust, drag and wake structure in flapping compliant membrane wings. J. Fluid Mech. 862, 871–888.
Waldman, R.M., Breuer, K.S., 2013. Shape, lift, and vibrations of highly compliant membrane wings. In: 43rd AIAA Fluid Dynamics Conference. p. 3177.
Waldman, R.M., Breuer, K.S., 2017. Camber and aerodynamic performance of compliant membrane wings. J. Fluids Struct. 68, 390–402.
Watanabe, Y., Suzuki, S., Sugihara, M., Sueoka, Y., 2002. An experimental study of paper flutter. J. Fluids Struct. 16 (4), 529–542.
Yang, S., Sultan, C., 2016. Modeling of tensegrity-membrane systems. Int. J. Solids Struct. 82, 125–143.
Zhang, J., Childress, S., Libchaber, A., Shelley, M., 2000. Flexible filaments in a flowing soap film as a model for one-dimensional flags in a two-dimensional wind. Nature 408 (6814), 835–839.
Zhao, W., Païdoussis, M.P., Tang, L., Liu, M., Jiang, J., 2012. Theoretical and experimental investigations of the dynamics of cantilevered flexible plates subjected to axial flow. J. Sound Vib. 331 (3), 575–587.
Zhu, L., Peskin, C.S., 2002. Simulation of a flapping flexible filament in a flowing soap film by the immersed boundary method. J. Comput. Phys. 179 (2), 452–468.